Received: 15 September 2020 | Revised: 13 July 2021 | Accepted: 22 July 2021

DOI: 10.1111/bre.12594

RESEARCH ARTICLE

Basin Research | IAS EAGE | WILEY

Syn-rift hydrothermal circulation in the Mesozoic carbonates of the western Adriatic continental palaeomargin (Western Southalpine Domain, NW Italy)

L. Barale[1] | **C. Bertok**[2] | **A. d'Atri**[1,2] | **A. Mantovani**[2] | **L. Martire**[2] | **S. Agostini**[3] | **S. M. Bernasconi**[4] | **A. Gerdes**[5] | **S. Ferrando**[2]

[1]Torino Unit, National Research Council of Italy, Institute of Geosciences and Earth Resources, Torino, Italy

[2]Department of Earth Sciences, University of Torino, Torino, Italy

[3]National Research Council of Italy, Institute of Geosciences and Earth Resources, Pisa, Italy

[4]Department of Earth Sciences, ETH Zurich, Zurich, Switzerland

[5]Department of Geosciences, Goethe University Frankfurt, Frankfurt am Main, Germany

Correspondence
Carlo Bertok, Department of Earth Sciences, University of Torino, Torino, Italy.
Email: carlo.bertok@unito.it

Funding information
University of Torino; Compagnia di San Paolo; National Research Council of Italy, Institute of Geosciences and Earth Resources, Torino Unit

Abstract

Evidence of hydrothermal activity is reported for the Mesozoic pre- and syn-rift successions of the western Adriatic palaeomargin of the Alpine Tethys, preserved in the Western Southalpine Domain (NW Italy). The products of hydrothermal processes are represented by vein and breccia cements, as well as dolomitization and silicification of the host rocks. In the eastern part of the study area, interpreted as part of the necking zone of the continental margin, Middle Triassic dolostones and Lower Jurassic sediments are crossed by veins and hydrofracturing breccias cemented by saddle dolomite. The precipitation of dolomite cements occurred within the stratigraphic succession close to the sediment–water interface. Despite the shallow burial depth, fluid inclusion microthermometry and clumped isotopes show that hydrothermal fluids were relatively hot (80–150°C). In the western part of the study area, interpreted as part of the hyperextended distal zone, a polyphase history of host-rock fracturing is recorded, with at least two generations of veins cemented by calcite, dolomite and quartz. Vein opening and cementation occurred at shallow burial depth around the time of deposition of the syn-rift clastic succession. Fluid inclusion microthermometry on both quartz and dolomite cements indicates a fluid temperature of 90–130°C, again pointing to hydrothermal fluids. Both in Fenera-Sostegno and Montalto Dora areas, O, C and Sr isotope values, coupled with fluid inclusion and clumped isotope data, indicate that hydrothermal fluids derived from seawater interacted with crustal rocks during hydrothermal circulation. Stratigraphic and petrographic evidence, and U–Pb dating of dolomitized clasts within syn-rift sediments, document that hydrothermal fluids circulated through sediments from the latest Triassic to the Toarcian, corresponding to the entire syn-rift evolution of the western portion of the Adriatic palaeomargin. The documented hydrothermal processes are temporally correlated with regional-scale thermal events that took place in the same time interval at deeper crustal levels.

KEYWORDS

fault-related fluid circulation, hydrothermal fluids, hyperextended distal margin, necking zone, Southalpine Domain

1 | INTRODUCTION

Fluid circulation in the continental crust is an active and effective process (e.g. Pirajno, 2009; Yardley & Bodnar, 2014). Fluids are highly diverse with respect to temperature, origin, chemical composition, circulation pathways and mechanisms depending on the tectonic context. They are of paramount importance in heat and mass transfer (e.g. transporting base metals leached from deeply seated basement rocks to overlying sedimentary rock units; Yardley, 2005) and in diagenetic processes such as dissolution, cementation and replacement (among which notably dolomitization and silicification), which may take place at any stage of the post-depositional to deep burial history of a sedimentary succession.

Typical fluid flow regimes in sedimentary basins include: gravity-driven downward movement of meteoric or hypersaline, evaporated seawater; compaction-driven, upward flux of connate waters squeezed from buried sediments and thermo-baric upward flow involving mineral-bound water released by mineral dehydration (e.g. gypsum, clays) when sufficiently high temperatures are reached during deep burial (e.g. Bjørlykke, 1993, 2010). Temperature gradients between the top and the bottom of thick highly permeable aquifers, not interbedded with aquitards, may trigger convection cells. At a larger scale, crystalline basement rocks may play an important role in chemical exchange and heat transfer, when their permeability allows water to flow through them. Faults and the associated fracture systems are preferential conduits for both downward and upward fluid circulation. Meteoric or marine waters can flow downwards, penetrate within buried rocks for several kilometres and subsequently, after heating, ascend along faults and fractures, which can eventually breach to the surface giving rise to subaerial or submarine thermal springs. For example, up to 10 km of penetration of meteoric waters in the Alps was documented by Diamond et al. (2018). The original fluid composition is commonly modified by several processes such as organic matter degradation and hydrocarbon production, mineral dehydration and water–rock interaction (including dissolution of evaporites, or alteration of silicate minerals of basement crystalline rocks or of clastic sediments; e.g. Bjørlykke, 1993, 2010; Clayton et al., 1966; Hitchon & Friedman, 1969; Land & Prezbindowski, 1981). An additional potential source of fluids is provided by magmatic and metamorphic processes, which can locally and importantly influence chemical and physical characteristics of the fluid circulating through sedimentary rock units (e.g. serpentinization of peridotite at mantle exhumation sites, Debure et al., 2019; Pinto et al., 2017; Salardon et al., 2017).

It is well documented that rift systems, forming in an extensional regime with formation of complex, normal and strike-slip transfer faults associations, are mostly favourable to generating deeply penetrating high-angle permeable fracture zones, which work as conduits for both down- and upward fluid flow (e.g. Hirani et al., 2018; Incerpi, Manatschal, et al., 2020; Incerpi, Martire, et al., 2020; Pinto et al., 2017; Salomon et al., 2020).

Highlights

- Widespread hydrothermal fluid circulation occurred in the upper crust of the Adriatic palaeomargin;
- Hydrothermal fluids were hot (80–150°C), overpressured and circulated along faults in a shallow burial setting;
- Multiple hydrothermal events occurred during all the stages of the Late Triassic–Jurassic extensional rifting and
- A compositional evolution of the hydrothermal fluids reflects different flow paths in the upper crust.

Dolomitization, a still open problem in geology, is a diagenetic process, which affects very large rock volumes and is related to massive flow of fluids. According to the accepted models of dolomitization (e.g. Machel, 2004; Warren, 2000 and references therein), these fluids may originate from sinking, dense, strongly evaporated seawater in hypersaline marginal environments, from thermal convection of normal seawater or from compactional flow of fluids, whose composition has been significantly modified during burial. In some instances, it can be demonstrated that dolomitizing fluids were, actually, hydrothermal fluids, that is, fluids with a higher temperature than the surrounding rocks. The importance of hydrothermal dolomitization, often associated with ore deposits – the well-known Mississippi valley-type deposits –, has been widely recognized in the last 15 years (e.g. Davies & Smith, 2006; Leach et al., 2010; Motte et al., 2021; Paradis et al., 2007). Dolomite, and commonly associated sulphides, in these cases most likely formed in carbonate bodies long after deposition of the precursor calcareous sediment. However, it is becoming increasingly clear, combining old and new analytical techniques (such as fluid inclusion microthermometry, clumped isotopes and U/Pb geochronology on carbonate minerals; Barale et al., 2021; Brigaud et al., 2020; Elisha et al., 2020; Incerpi, Manatschal, et al., 2020; Incerpi, Martire, et al., 2020; Mangenot et al., 2018; Salih et al., 2019), that many dolostones are formed at high temperature, but shortly after deposition of the host sediments, that is, at shallow burial depths or even at near-surface conditions (Barale et al., 2016; Shelton et al., 2019). Rift settings provide two crucial elements favourable to such type of dolomitization: fault and associated fracture systems as conduits for downward and upward fluid flow, and high heat flow

due to crustal thinning (Haeri Ardakani et al., 2013; Hirani et al., 2018; Hollis et al., 2017; López-Horgue et al., 2010; Martín-Martín et al., 2015; Shelton et al., 2019; Swennen et al., 2012). Moreover, in distal hyperextended continental margins, where mantle exhumation takes place, serpentinization of peridotite can result in production of Mg-enriched fluids, which can further enhance dolomitization of overlying carbonate formations (Debure et al., 2019; Lagabrielle et al., 2019). In the same distal setting, a change in the chemistry of fluids, and of the resulting diagenetic products (from carbonate to silica dominated), has been recently reported at the transition between a first rift stage of crustal stretching to a second one characterized by low-angle detachment faults that determined hyperextension and thinning of the continental crust (Incerpi, Manatschal, et al., 2020; Incerpi et al., 2017, 2018; Incerpi, Martire, et al., 2020; Masini et al., 2013; Mohn et al., 2010).

The purpose of this study is to investigate, with a multidisciplinary approach, the pre- to syn-rift sedimentary successions of the Western Southalpine Domain, a portion of the Alpine chain where the metamorphic overprint is very slight or completely absent. Therefore, it preserves the signature of the flow of fluids related to tectonic activity present during the individualization of the Adriatic continental margin and the transition to mantle exhumation and birth of the Liguria–Piemonte ocean. In particular, according to the last interpretations (Beltrando et al., 2015; Decarlis et al., 2017; Ferrando et al., 2004), the study sector exposes the transition from the necking zone of the Mesozoic Adriatic continental margin to its distal part. Pre- to syn-rift, mainly carbonate sediments of such successions, are highly sensitive to the flow of hot fluids, and thus, offer the opportunity to gain information on the occurrence, features, timing and spatial evolution of the related hydrothermal systems. This information allowed to improve our understanding of time and space variations of tectonically controlled fluid circulation in rifted continental margins, confirming the model recently defined in a different sector of the same palaeomargin (Incerpi et al., 2017; Incerpi, Martire, et al., 2020).

2 | GEOLOGICAL SETTING

The Adriatic palaeomargin of the Alpine Tethys experienced an Early Jurassic rifting, which ultimately led to the lithosphere break-up and production of the first oceanic crust in the Middle Jurassic. The rifting evolution lasted about 30–40 Myr, but extensional tectonic movements were non-continuous and not equally distributed in space. A first diffuse rifting stage, in the Hettangian–Sinemurian, generated half-graben basins characterized by high subsidence and deposition rates in the Central Southalpine Domain (e.g. Monte Generoso basin; Bernoulli, 1964; Bertotti et al., 1993). In the late Pliensbachian–Toarcian, tectonic activity decreased and ceased in this domain, and focused westward, to the Western Southalpine Domain. In the eastern part of this domain, which in the Hettangian–Sinemurian had acted as a structural high bordering the rapidly subsiding Lombardy Basin, mainly N–S striking listric faults generated small basins, the Monte Fenera and Sostegno Basins (Figure 1b,c) (Beltrando et al., 2015; Berra et al., 2009; Decarlis et al., 2017). The contemporaneous activity of low-angle shear zones cutting the entire crust (e.g. the Pogallo Line; Handy, 1987) determined the necking of the crust, which progressively thinned out westward towards the more distal, hyperextended, portion of the margin. This is now exposed in the Canavese zone and, in particular, in the Montalto Dora area (Figure 1). Here, low-angle extensional detachment faults led to the exhumation of rocks of the upper and lower crust at the seafloor (Ferrando et al., 2004).

The Mesozoic succession of the Monte Fenera–Sostegno area (Berra et al., 2009; Fantoni et al., 2003; Govi, 1975. See Figure 2a,b) rests on Permian volcanites and starts with a few metres of shallow-marine sediments (Fenera Annunziata Sandstone), followed by 200–300 metres of fine-grained peritidal carbonates (San Salvatore Dolostone, late Anisian–Ladinian; hereafter named SSD), largely affected by a syn-depositional to very early diagenetic dolomitization. The uppermost part of the SSD is crossed by neptunian dykes. In the Sostegno area, they are up to a few tens of centimetres wide and several metres deep, and they are filled with a fine-grained reddish sediment. The top of the SSD is marked by an erosional surface, likely related to subaerial exposure and corresponding to a stratigraphic gap spanning the Late Triassic and part of the Early Jurassic. The unconformity is covered by the sediments of the San Quirico Sandstone (late Pliensbachian; hereafter named SQS). The SQS starts with a few tens of centimetres thick, laterally discontinuous interval of coarse sandstones to micro-conglomerates with clasts of SSD and a reddish fine-grained matrix (corresponding to the 'Monte Fenera Breccia' of Fantoni et al., 2003). This is followed by shallow-marine lithic sandstones rich in clasts of SSD and Permian volcanics. The SQS is in turn overlain by spiculitic limestones and marls with interbedded resedimented sandstones (Calcari Spongolitici, Toarcian). These successions are only slightly affected by Alpine tectonics and experienced maximum burial temperatures of 60–70°C, as revealed by organic matter maturity (Fantoni & Scotti, 2003).

The Montalto Dora area is presently incorporated into a several kilometre-wide tectonic deformation zone, the Canavese Zone, which samples the distal part of the Adriatic palaeocontinental margin (Beltrando et al., 2015; Ferrando et al., 2004; Piana, Fioraso, et al., 2017; Piana, Barale et al., 2017). It is bounded by two tectonic lines, the external and internal Canavese Lines, which juxtapose the Montalto Dora area to the eclogitic Sesia–Lanzo rocks to the north,

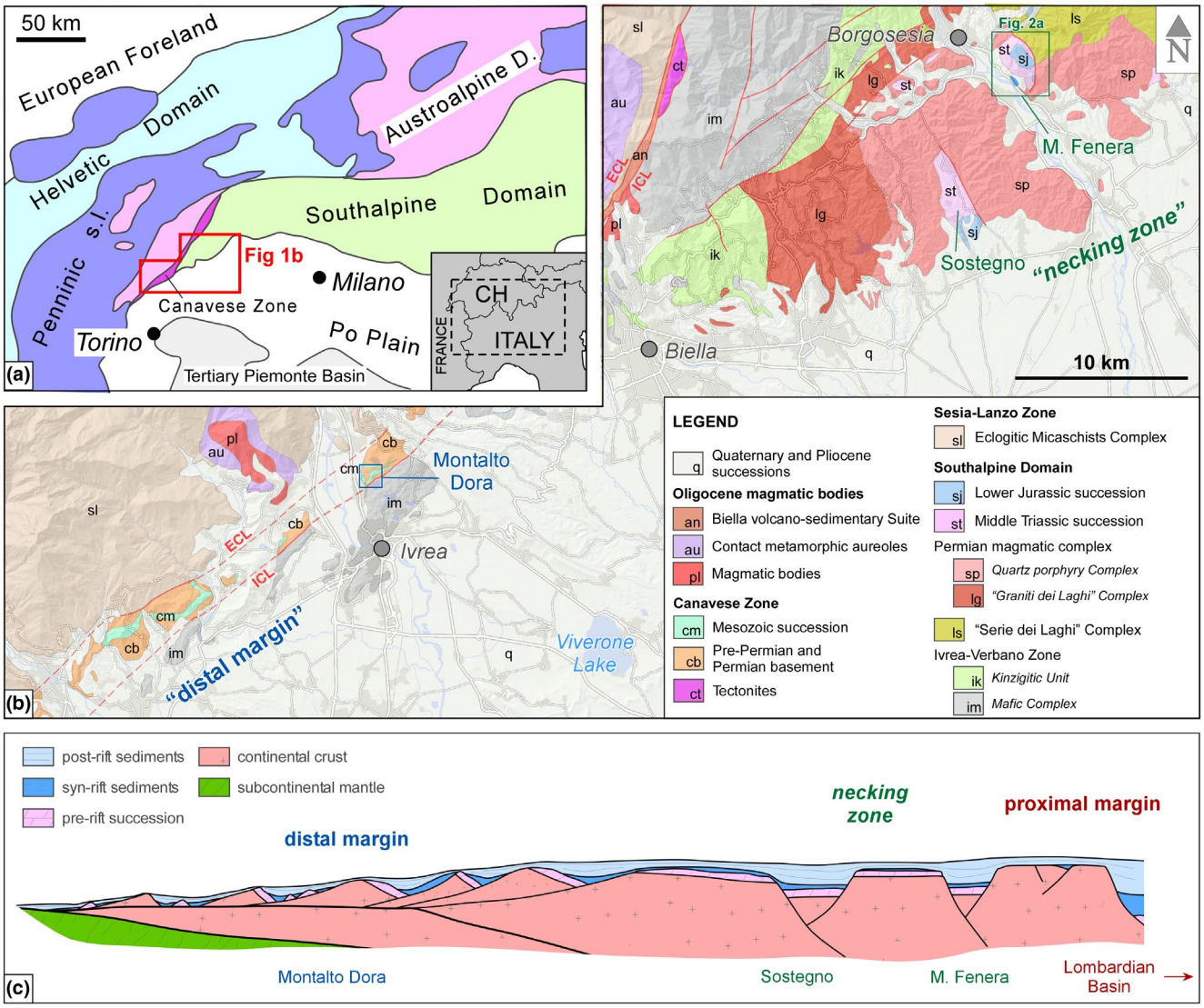

FIGURE 1 (a) Geological sketch of the Western and Central Alps. The study area (red polygon) lies at the westernmost end of the Southalpine Domain. (b) Simplified geological map of the study area; modified from Piana, Fioraso, et al. (2017); ICL, Internal Canavese Line; ECL, External Canavese Line. (c) Ideal cross section across the Adriatic palaeomargin in the Middle Jurassic (partly modified from Beltrando et al., 2015; Ferrando et al., 2004), showing the relative positions of the studied outcrops

and to the mafic lower crust of the Ivrea–Verbano zone to the south (Biino & Compagnoni, 1989). The Montalto Dora area consists of a crystalline basement composed of Variscan low-grade metamorphic rocks (phyllite, metabasite and paragneiss with minor orthogneiss and impure quartzite) intruded by lower Permian granitoids (diorite to quartz diorite and leucogranite). The basement is overlain by lower Permian volcanics and upper Permian volcanoclastic rocks ('Verrucano', Baggio, 1965). Recently, Festa et al. (2020) documented the great complexity of the pre-Triassic substrate related to polyphase tectonics mainly of Variscan age. Triassic sediments are represented by few tens of metres of Middle Triassic massive dolostones (San Salvatore Dolostone-SSD; Elter et al., 1966), locally crossed by neptunian dykes with a complex polyphase filling, represented by pinkish encrinites, dolostone breccias with a reddish arenitic matrix, red or greenish shales and sandstones (Baggio, 1965; Elter et al., 1966). The pinkish encrinites were dated to the earliest Sinemurian by Sturani (1964), on the basis of a single ammonite specimen. All infilling sediments also locally occur as thin and discontinuous levels directly on the top of the SSD (Elter et al., 1966). The SSD is overlain by Lower Jurassic dark sandstones and shales, followed by interbedded limestones and shales (Lago Pistono and Bio' Schists, Biino & Compagnoni, 1989), of probable Middle Jurassic age.

Berra et al. (2009), on the basis of the lithological features, stressed the close affinities of the Triassic succession with that of the Monte Fenera area. Recently, Festa et al. (2020) documented the direct superposition of the Middle Triassic dolostones on the Lower Permian volcanites, due to the

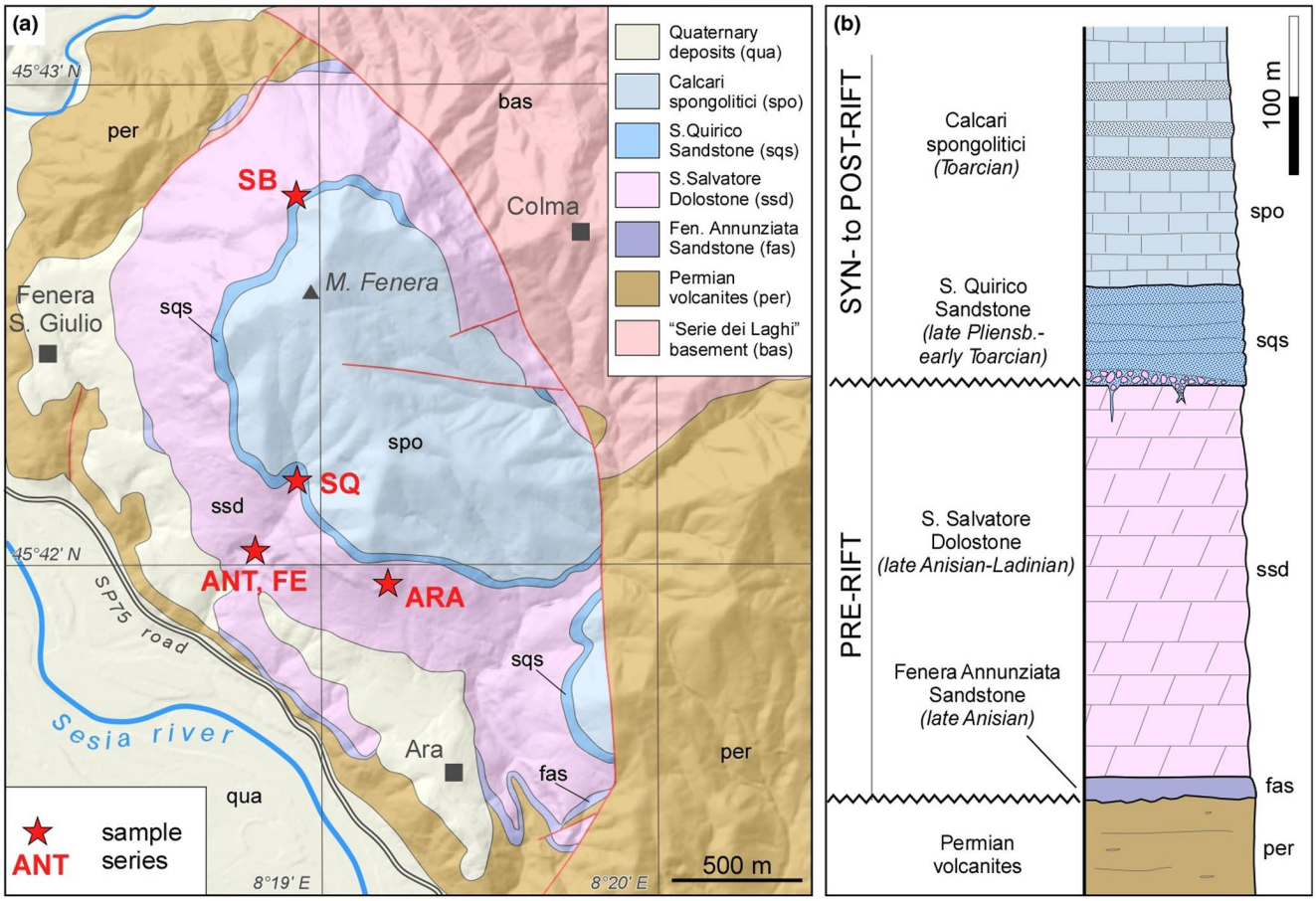

FIGURE 2 (a) Geological scheme of the Monte Fenera area (after Govi, 1975); the collection sites of the samples series ANT, ARA, FE, SB and SQ are shown. (b) Stratigraphic succession of Monte Fenera

absence of the Upper Permian 'Verrucano' sediments in the Montalto sector of the Canavese Zone. The top of the SSD is overlain by a few metres of breccia (Arenaceous Member, MUF-AM) followed by alternating limestone and sandstone (Limestone Member, MUF-LM), tentatively attributed to the late Early–Middle Jurassic and informally named as Muriaglio Formation (Festa et al., 2020). The Montalto Dora area corresponds to a strike-slip deformation zone, internally subdivided into lense-shaped hectometre-sized rock bodies, bounded by ENE- to NE and E-striking faults (Festa et al., 2020), which hinders to laterally follow the stratigraphic contacts over great distances. A prehnite–pumpellyite–actinolite facies Alpine metamorphism has been reported in the basement rocks (approximately 250–300°C; Biino & Compagnoni, 1989).

3 | MATERIALS AND METHODS

3.1 | Petrography

Petrographic studies on uncovered thin sections (30 μm thick) were carried out by optical microscopy and cathodoluminescence (CL) at the Department of Earth Sciences, University of Torino. CL observations were carried out using a CITL 8,200 mk^3 equipment (operating conditions of about 17 kV and 400 μA).

3.2 | Fluid inclusion study

Fluid inclusion petrography was carried out on bi-polished 80-μm-thick thin sections. Microthermometry of primary fluid inclusions in dolomite and quartz was performed at the Department of Earth Sciences, University of Torino, using a Linkam THMSG600 heating–freezing stage coupled with an Olympus polarizing microscope (100× objective), using the standard method described by Goldstein and Reynolds (1994). Crystal size classes used in dolomite description are those proposed by Folk (1962).

3.3 | δ^{13}C and δ^{18}O

Carbon and oxygen isotopic compositions of the carbonates were measured at the Stable Isotope Laboratory of the ETH Geological Institute (Zurich, Switzerland) using a Thermo

Fisher Scientific GasBench II coupled to a Delta V mass spectrometer, as described in Breitenbach and Bernasconi (2011). The oxygen isotope composition of dolomite was calculated using the fractionation factor of Rosenbaum and Sheppard (1986). The isotopic ratios for carbon and oxygen are expressed as $\delta^{13}C$ and $\delta^{18}O$ per mil values relative to the VPDB (Vienna Pee Dee Belemnite) standard, with average reproducibility of ±0.05‰ for both $\delta^{13}C$ and $\delta^{18}O$.

3.4 | Carbonate clumped C–O isotopes

The clumped isotope composition of dolomite and calcite was determined at the ETH Zurich using a Thermo Fisher Scientific 253Plus mass spectrometer coupled to a Kiel IV carbonate preparation device, following the method described in Meckler et al. (2014) and Müller et al. (2017). The Kiel IV device includes a custom-built Porapak Q trap held at −40°C to eliminate potential organic contaminants. Prior to each sample run, the pressure-dependent negative backgrounds are determined on all beams to correct for non-linearity effects. During each run, 18 replicates of 90–110 µg of different samples and 5 replicates of each of the 3 carbonate standards, ETH-1, ETH-2 and 8 replicates of ETH-3 (Bernasconi et al., 2018), are analysed for data normalization. Two replicates of the international standard IAEA C2 are analysed to monitor the long- term reproducibility of the instrument. All instrumental and data corrections are carried out with the software Easotope (John & Bowen, 2016) using the revised IUPAC parameters for ^{17}O correction (Bernasconi et al., 2018). Clumped isotopes for dolomite are reported in the carbon dioxide equilibration scale (CDES) phosphoric acid reaction temperature of 70°C, whereas those of calcite are reported for a reaction temperature of 25°C. Temperature uncertainties are reported at the 95% confidence level (Bernasconi et al., 2018; Fernandez et al., 2017). Δ47 temperatures and isotopic composition of waters in equilibrium with the dolomite are calculated with the dolomite-specific calibrations of Müller et al., 2019. For calcite, we used the calibration in Bernasconi et al. (2018). The composition of the fluids was calculated using the oxygen isotope calibration of O'Neil et al. (1969).

3.5 | Sr isotopes

Sr isotopic analyses of five samples were performed using a ThermoFisher Neptune Plus MC-ICP-MS at the Institute of Geosciences and Earth Resources of CNR (Pisa, Italy), in 2% HNO_3 solution containing 20–200 ng/g of analyte, after Sr extraction from matrix in class 100 clean room using the specific Sr-spec resin Eichrom Sr. The instrument was equipped with a combined cyclonic and Scott-type quartz spray chamber, Ni-cones and a MicroFlow PFA 100 µl/min self-aspiring nebulizer. Sr analyses were corrected for mass bias fractionation using the $^{88}Sr/^{86}Sr$ ratio (= 8.375209) and for mass interference using the ratios $^{83}Kr/^{84}Kr$ (= 0.201750), $^{83}Kr/^{86}Kr$ (= 0.664740) and $^{85}Rb/^{87}Rb$ (= 2.592310). The analytical accuracy and long-term external reproducibility for $^{87}Sr/^{86}Sr$ of reference material NIST SRM 987 was 0.710251 ± 12 (n = 38). The rock standard AGV-1 was also measured during sample measurement, with a result of $^{87}Sr/^{86}Sr$=0.704023 ± 10 (long-term reproducibility for $^{87}Sr/^{86}Sr$ of AGV-1 was 0.704014 ± 15, n = 15).

3.6 | U–Pb dating

Uranium–lead data were acquired in situ on polished thin sections from different samples by laser ablation inductively coupled plasma-mass spectrometry (LA-ICP-MS) at the Goethe University Frankfurt (GUF), using a method modified by Gerdes and Zeh (2006, 2009). At GUF, a Thermo Scientific Element 2 sector field ICP-MS is coupled to a Resolution S-155 (Resonetics) 193 nm ArF Excimer laser (CompexPro 102, Coherent) equipped with a two-volume ablation cell (Laurin Technic, Australia). Samples were ablated in a helium atmosphere (0.6 L/min) and mixed in the ablation funnel with 0.7 L/min argon and 0.04 L/min nitrogen. Signal strength at the ICP-MS was tuned for maximum sensitivity while keeping oxide formation below 0.3% (UO/U). Static ablation used a spot size of 213 µm and a fluence of <1 J/cm^2 at 6 Hz. This yielded for SRM-NIST 614, a depth penetration of about 0.5 µm/s and an average sensitivity of 420,000 cps/(µg/g) for ^{238}U. The detection limits for ^{206}Pb and ^{238}U were ca. 0.1 and 0.03 ppb respectively. However, at a U signal of less than 1,000 cps (ca. 2 ppb), the data were generally discarded due to enhanced scatter on the isotope ratios.

Each analysis consisted of 20 s background acquisition followed by 20 s of sample ablation and 25 s washout. During 42 s data acquisition, the signal of ^{206}Pb, ^{207}Pb, ^{208}Pb, ^{232}Th and ^{238}U was detected by peak jumping in pulse counting mode with a total integration time of 0.1 s, resulting in 420 mass scans. Prior to analysis, each spot was pre-ablated for 3 s to remove surface contamination. Soda-lime glass SRM-NIST 614 was used as a reference glass together with two carbonate standards to bracket sample analysis.

Raw data were corrected offline using an in-house MS Excel© spreadsheet program (Gerdes & Zeh, 2006, 2009). Following background correction, outliers (±2σ, standard deviation) were rejected based on the time-resolved $^{207}Pb/^{206}Pb$ and $^{206}Pb/^{238}U$ ratios. The $^{207}Pb/^{206}Pb$ ratio was corrected for mass bias (0.3%) and the $^{206}Pb/^{238}U$ ratio for inter-element fraction (ca. 5%), including drift over the 12 hr of sequence time, using SRM-NIST 614. Due to the carbonate matrix, an additional correction of 3% has been applied on the $^{206}Pb/^{238\,U}$, which was determined using WC-1 carbonate reference material dated by

TIMS (254.4 Ma; Roberts et al., 2017). A total of 34 runs of the WC-1 carbonate standard over the course of the two analytical sessions provided a lower intercept age of 254.1 ± 1.1 Ma (2σ). Repeated analyses (n = 35) of a Zechstein dolomite (255 ± 4 Ma; Gypsum pit, Tettenborn, Germany), used as secondary (in-house) standard, yielded a lower intercept age of 256.0 ± 2.0 Ma (MSWD: 1.3), implying an accuracy and repeatability of the method of around 2% or better. Data were plotted in the Tera–Wasserburg diagram and ages calculated as lower intercepts using Isoplot 3.71 (Ludwig, 2009). All uncertainties are reported at the 2σ level.

4 | STRATIGRAPHY AND PETROGRAPHY

4.1 | Monte Fenera–Sostegno sector

The stratigraphic succession of the Monte Fenera–Sostegno sector has been revised recently (Berra et al., 2009; Fantoni et al., 2003). In this contribution, we will focus only on petrographic features so far undescribed and useful to reconstruct the diagenetic evolution. The dataset refers to samples collected in the lower part of the San Salvatore Dolostone (SSD) and in proximity of the SSD-San Quirico Sandstone (SQS) boundary (Monte Fenera, Figure 2a, and Sostegno).

At Monte Fenera (Figure 2a,b), the lower part of the SSD, whose facies consists of fine-grained massive and laminated dolostones, locally shows tabular, bedding-parallel breccia bodies, about 10 cm thick (Figure 3a). The breccias are clast -supported and clasts are cm-sized, angular, flat in shape and mainly parallel to bedding; more irregular shapes of the clasts are also observed. Spaces among the clasts show quite complex infillings with alternations of different generations of internal fine-grained sediments and dolomite cements to form multiphase geopetal structures (Figure 3b–f). Cathodoluminescence reveals a marked zoning of the dolomite cement, which in turn documents an unexpected complexity of the diagenetic phases. A first generation of dolomite (DOL1) occurs both as replacement of the first generation of internal sediment (SED1) and as a thin rim of cement encrusting the top of SED1. It shows a dull CL and a zoning with a reddish brown core, followed by a middle greenish zone and an outer brown zone. DOL1 is overgrown by a generation of coarser dolomite (DOL2) characterized by a distinctive CL zoning consisting of an inner non-luminescent (NL) zone, a middle zone where NL and bright yellow subzones alternate, and an outer thick zone, richer in inclusions, with a CL from moderate orange to dull brown or even NL. Locally, at the inner-middle zone boundary, irregular patches of bright red luminescing dolomite occur, likely referable to a later partial recrystallization. DOL2 is also seen in a nearly isopachous rim of cement with scalenohedral terminations about 200–400 micron thick locally overlain by a second generation of internal sediment (SED2). However, the CL zoning of DOL2 is markedly discordant with the external morphology of the crystals, thus documenting a dissolution of the former cement rim after deposition of SED2 and the precipitation of DOL2 in the resulting voids (Figures 3c,d and 4). In some cavities, DOL1 and DOL2 cements are separated by a sediment layer which represents a third stage of sediment infiltration in the open spaces of the breccia. The SSD, and the breccia bodies themselves, are further crossed by subvertical mm-large fractures cemented by different generations of coarsely crystalline dolomite, moderate orange to dull brown in CL (DOL3). Commonly, these veins also contain very thin seams of dolomitized red sediments (Figure 3b).

The uppermost part of the SSD displays a network of mm-thick dykes filled with finely dolomitized red sediments. M m-thick, sharp-edged fractures, cemented by dolomite, cross cut the dolostones and the dykes (Figure 5a–c). When entering the overlying SQS, these fractures pass to irregularly shaped ‘conduits’ and cavities, cemented by coarsely crystalline, locally saddle, dolomite. These cavities do not cross the pebbles of the SQS but ‘make their way’ around them, and thus, were probably opened in a semi-consolidated sediment (Figure 6). Along these ‘conduits’, the spaces among clasts, normally filled with a reddish, finely dolomitized sediment, are either plugged by coarsely crystalline dolomite or by both sediment and dolomite cement (Figure 5b,c). This dolomite cement shows a CL cement stratigraphy (DOL1 and DOL2) comparable with that described in the lower part of the SSD.

At Sostegno, the top of the SSD is crossed by larger and more deeply penetrating fissures which are mainly bedding parallel, and mm-to-dm thick (Figure 7a). They are filled with brick red finely dolomitized sediments locally laminated and including angular cm-sized clasts of the encasing SSD. Several cm-sized cavities, with lobed edges, are found within the red sediments filling the fissures, and mm-thick bleached halos of yellowish colour occur at the red sediment-cement boundary. The cavities are locally more abundant and connected to each other in dm-sized, subvertical belts where the red sediment is disrupted into rounded cm-large clasts (Figure 7b). The cavities are cemented by extremely coarsely crystalline saddle dolomite, locally growing into scimitar-like crystals (Figure 7c). The dolomite cements show a CL pattern with a first interval with alternating non-luminescent to orange-red thin zones, followed by a much thicker interval, internally less zoned and ranging from moderate orange to dull brown. This dolomite cement stratigraphy is closely comparable to that observed in the DOL2 cements at Monte Fenera. Sand-sized dolomite grains occur in the red sediments: they are characterized by a very distinctive CL zoning, with a greenish irregularly shaped core surrounded by a syntaxial rim with non-luminescent to orange-red thin

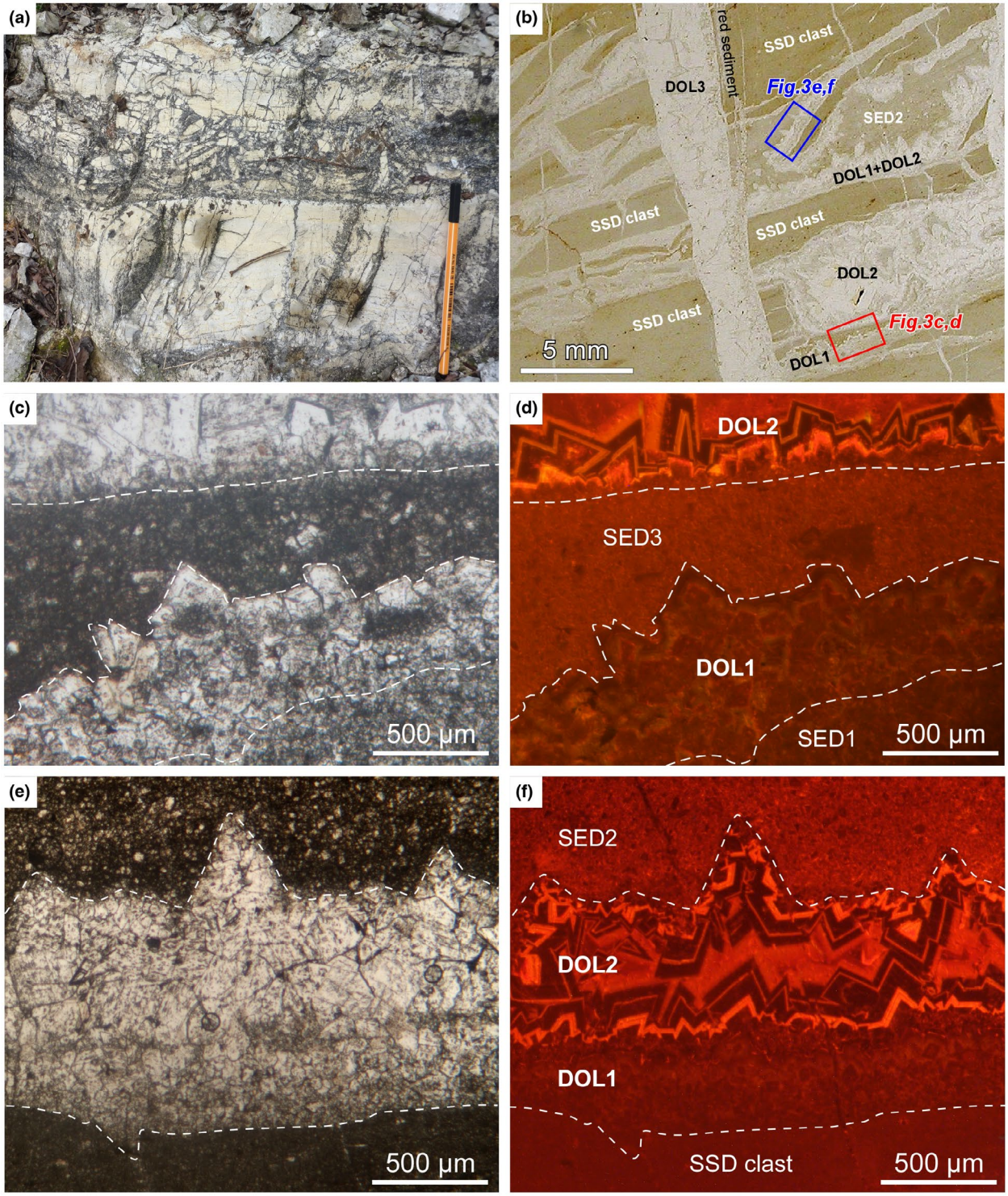

FIGURE 3 Monte Fenera area. (a) Tabular, bedding-parallel breccia body in the lower part of the SSD. Although the aspect of this breccia mimics the transgressive breccias at the base of peritidal cycles, its internal complexity, better seen in thin section and displayed in Figure 3b-f, shows that it is likely related to hydrofracturing. Pen for scale is 16 cm long. (b) Photomicrograph of Figure 3a breccia (transmitted, plane polarized light), showing the complex, polyphase infillings of the voids between the SSD clasts. Note that adjacent cavities show different infillings. The breccia is lastly crossed by subvertical mm-large fractures cemented by DOL3. Sample FE2 (for location, see Figure 2a). (c–f) Details of (b) (c, e, plane polarized light; d, f, cathodoluminescence). (c and d) The first dolomite cement DOL1, with a moderate-to-dull CL, overlies the first internal sediment (SED1) flooring the breccia cavities and is in turn overlain by another internal sediment (SED3) and dolomite cement DOL2, which completely fills the pore. (e and f) DOL1 and DOL2 cements are directly superposed and followed by an internal sediment (SED2) stopping the growth of DOL2. Note that the zoning of DOL2 is markedly discordant with the external morphology of cement crystals. For more details about the relative age of internal sediments, see Figure 4

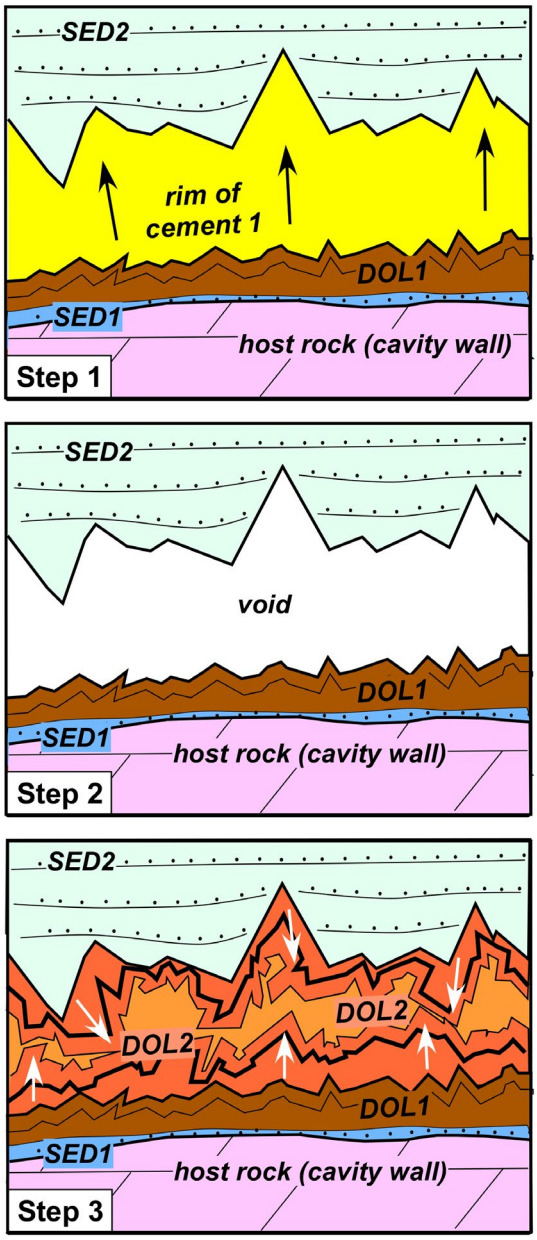

FIGURE 4 Interpretive sketch of the different episodes of cement precipitation and dissolution leading to the complex cement stratigraphy observed in the voids of the hydrofracturing-related breccia bodies at the base of the SSD at Fenera, and represented in Figure 5. Step 1: after opening of voids, likely due to hydrofracturing, the open spaces between the clasts have been infiltrated by a first generation of internal sediment (SED1), overgrown by a first dolomite cement rim (DOL1) and a coarsely crystalline cement rim (probably radiaxial calcite, CC1), in turn overlain by a second internal sediment (SED2); Step 2: the CC1 cement has been dissolved, leaving cavities mimicking the habit of the former crystals, and probably preserved thanks to the fact that SED2 was already semi-consolidated; Step 3: the voids have been centripetally filled with a new dolomite cement (DOL2). DOL1 and DOL2 cements, here directly superposed but clearly recognizable in CL, in other cavities, as that of Figure 3c,d, are separated by an internal sediment. It followed dissolution of the calcite cement and can thus be labelled as internal sediment 3

zones (closely similar to the first interval of the dolomite cements), developing a subhedral-to-euhedral rhombic habit (Figure 7d). These grains closely resemble those described by Martire et al. (2014) in the external Ligurian Briançonnais Middle Jurassic succession, and are similarly interpreted as diagenetic overgrowths of detrital monocrystalline dolomite grains.

4.2 | Montalto Dora sector

Apart from the metamorphic crystalline basement, the oldest rocks in the Montalto Dora area are Lower Permian volcanic and volcanoclastic rocks (Figure 8). The Upper Permian 'Verrucano' sediments are missing. The Middle Triassic San Salvatore Dolostone occurs as discontinuous decametre- to hectometre-sized, a few tens of metres thick rock bodies. These are overlain by a succession of mainly terrigenous sediments (Arenaceous member of the Muriaglio formation, MUF-AM following Festa et al., 2020) (Figure 9a) at most 15–20 m thick, which laterally, where the SSD is missing, directly lies on the Lower Permian volcanics. At the base of the MUF-AM, centimetre- to decimetre-thick beds of reddish and greenish interbedded coarse sandstones and breccias are present. The greenish beds are mainly composed of clasts of metamorphic rocks and the reddish ones of clasts of Lower Permian volcanic rocks (Figure 9b). These sediments pass upwards to greenish to reddish sandstones and shales with interbedded matrix-supported breccias with centimetre- to metre-sized SSD clasts and blocks (Figure 9c,d). The sandstones are composed, in order of abundance, of quartz grains, lithic fragments of volcanic rocks and dolostones, detrital white micas and feldspars. Minor components include titanite and apatite crystals and echinoderm fragments (Figure 9e–g). The uppermost part of the Muriaglio Formation is composed of interbedded dark micritic limestones, marls and subordinated fine-grained sandstones in thin beds (Limestone member, MUF-LM).

The uppermost part of the SSD is crossed by a complex network of centimetre- to metre-wide neptunian dykes. These are filled with matrix- or clast-supported breccias with millimetre- to decimetre-sized clasts of the SSD, of pinkish encrinitic limestones (Figure 10a), and of a reddish-to-greenish shaly-to-arenaceous matrix with the same petrographic features described above for the MUF-AM. In the following, we will refer to the latter also to indicate the dyke infillings.

The SSD, both in normal stratigraphic succession or as clasts in neptunian dikes or within the Muriaglio Formation, varies from very fine-grained mimetic dolostones with recognizable original allochems of the precursor calcareous sediments, to coarsely crystalline (up to 0.25 mm) fabric-destructive dolostones (Figure 9e) consisting of crystals with cloudy cores and limpid rims. In

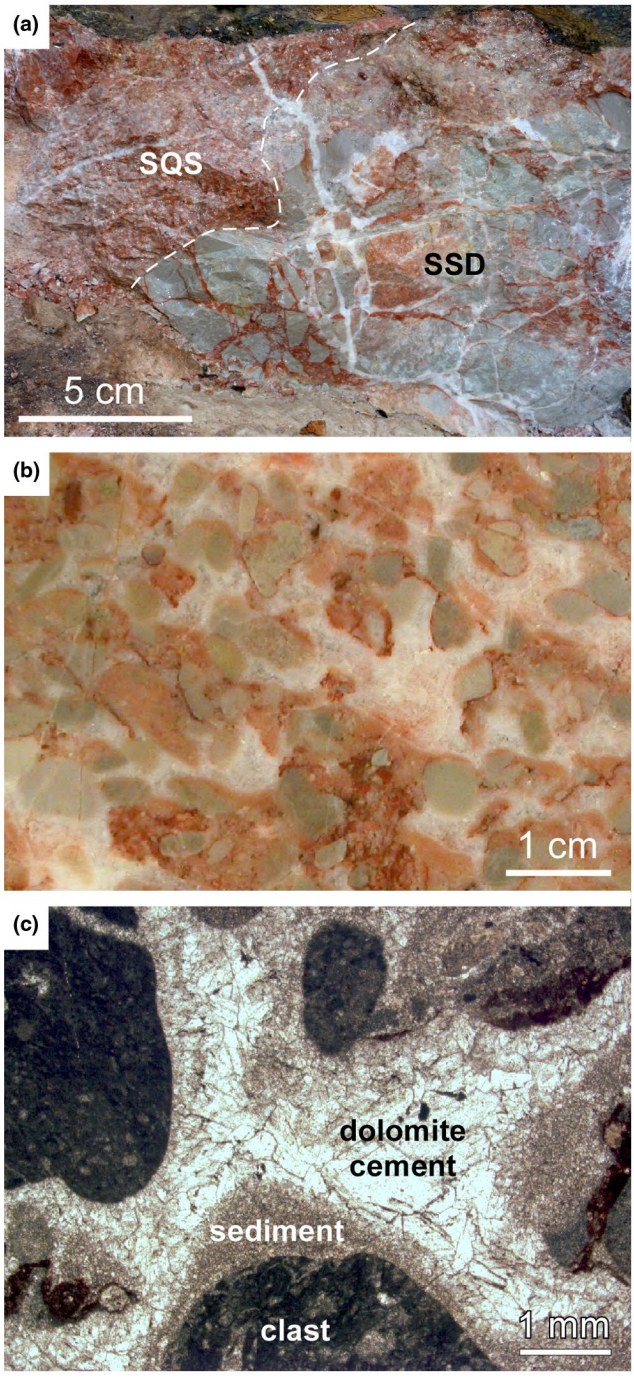

FIGURE 5 Monte Fenera area. (a) Stratigraphic boundary between SSD and the overlying SQS. The top of the SSD is crossed by a network of mm-thick dykes filled with finely dolomitized red sediments, in turn cross cut by mm-thick, dolomite-cemented fractures. Note that the latter also cross the SQS. (b) Polished sample of SQS just above the SSD–SQS boundary. Sample SQ6 (for location see Figure 2a). (c) Thin section detail (transmitted, plane polarized light) of the same sample. Irregular cavities plugged with reddish sediments and coarse white dolomite cements are clearly observable. Note that such cavities do not cross the clasts

cathodoluminescence, all dolostones show a prevailing dull brown colour but greenish luminescence also occurs (Figure 9g). Moreover, swarms of dolomite veinlets, micron to tens of microns thick, are clearly recognizable for the reddish-orange CL colour.

Some irregular millimetre- to centimetre-wide veins cross cut the SSD, and are filled with coarse saddle dolomite, quartz and calcite cements. They do not show a preferred orientation and locally form a dense network giving a brecciated aspect to the dolostones. Such veins also occur in SSD clasts in the MUF-AM, and abruptly stop at the edge of the clasts, clearly demonstrating that veining took place before deposition of the MUF-AM (Type 1 veins; Figures 10d–g and 12). Vein dolomite shows a CL zoning from non-luminescent to orange-red, and usually is the first filling cement. Locally, quartz is characterized by a fibrous habit, pointing to a syn-deformation crystal growth. Microcrystalline quartz is also present as replacement of the dolostone in irregularly shaped centimetre- to decimetre-sized patches that are locally cross cut by saddle dolomite veins. Silicified dolostone clasts also occur in the Muriaglio Formation. Sand-sized dolomite grains occur in the MUF-AM. They are characterized by a very distinctive CL zoning, with a greenish irregularly shaped core surrounded by a syntaxial rim with thin non-luminescent to orange-red zones, developing a subhedral-to-euhedral rhombic habit and closely resembling those at Sostegno (Figure 10h).

Quartz–calcite–dolomite veins, submillimetre to millimetre wide, cross cut both the dolostone clasts and the sandy matrix of the breccias at the base of the Muriaglio Formation. However, whereas they show sharp and straight edges in the clasts, in the matrix they are discontinuous, characterized by irregular margins and split in swarms of thinner veins (Type 2 veins, Figures 11a,b and 12). Dolomite overgrowths and Type 2 veins suggest a phase of fracturing and fluid circulation through the Muriaglio Formation shortly after its deposition, when its sediments were not still fully consolidated.

Locally, we observed a third group of veins (Type 3 veins, Figure 12) filled with calcite–dolomite and/or quartz and albite cements, which sharply cross-cut all lithotypes and previous vein generations. Since these veins clearly post-date the tectono-stratigraphic events considered in this study, and no geometric or stratigraphic constraint for their dating is available, they have not been investigated in detail.

5 | FLUID INCLUSION AND GEOCHEMICAL RESULTS

5.1 | Fluid inclusions

Fluid inclusions from eight samples from the Monte Fenera–Sostegno sector and the Montalto Dora sector have

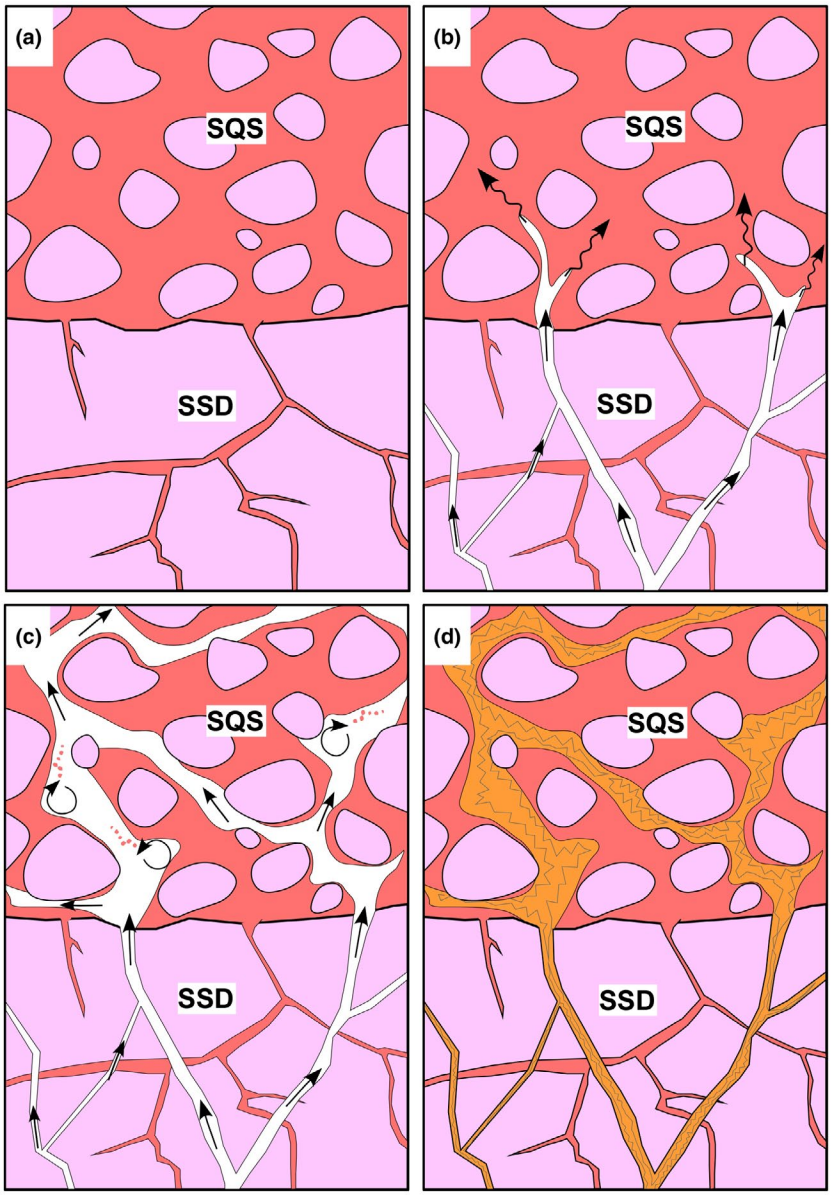

FIGURE 6 Interpretive sketch of the different steps leading to the features observed at the SSD–SQS boundary in the Monte Fenera area (see Figure 5). (a and b) Hydrofracturing-related opening of veins at the top of SSD occurred shortly after the deposition of the lower part of SQS, when these deposits were still not completely lithified. (c) Fluid flow resulted in the local, partial removal of the semi-consolidated matrix of the SQS, giving rise to a framework of irregular shaped cavities and conduits. (d) Cavities and conduits were cemented by coarsely crystalline dolomite

been studied (Table 1; see also File S1). Because of the small size of the fluid inclusions (a few microns), freezing runs to obtain information on fluid composition could not be performed. Only fluid inclusions of certain primary origin, occurring along crystal growth zones or as irregular isolated clusters, were analysed. They are two-phase inclusions, liquid rich with a vapour bubble, with irregular shapes and no evidence of stretching of either crystals or inclusions.

In the Monte Fenera–Sostegno sector, homogenization temperatures of fluid inclusions from DOL2 in the SSD and in the basal part of SQS range from 85 to 115°C. Only in sample ARA3, homogenization temperatures of DOL2 are considerably higher, ranging from 140 to 220°C (Figure 13). In the Montalto Dora samples, fluid inclusions occur in dolomite and quartz cements filling both Type 1 and Type 2 veins. Homogenization temperatures show a good clustering, with values on both Type 1 and Type 2 veins mostly ranging between 90 and 130°C (Figure 13).

5.2 | Stable and clumped isotopes

Twenty-four dolomite and two calcite samples were measured to determine their $\delta^{18}O$ and $\delta^{13}C$ (Table 1, Figure 14). In the Monte Fenera–Sostegno sector, two samples of the SSD show $\delta^{18}O$ values of −2.3‰ and −4.3‰. DOL2 cements show lower $\delta^{18}O$ values, ranging from −8.5‰ to −10.0‰. Three dolomitized internal sediments show $\delta^{18}O$ values of −1.6‰, −7.6‰ and −8.7‰. The $\delta^{13}C$ of all samples range from +1.0‰ to +3.7‰ VPDB, typical values of marine sediments. In the Montalto Dora sector, two samples of the finely crystalline SSD show $\delta^{18}O$ values of −4.9‰ and −5.1‰, whereas three samples of coarsely crystalline SSD clasts yielded

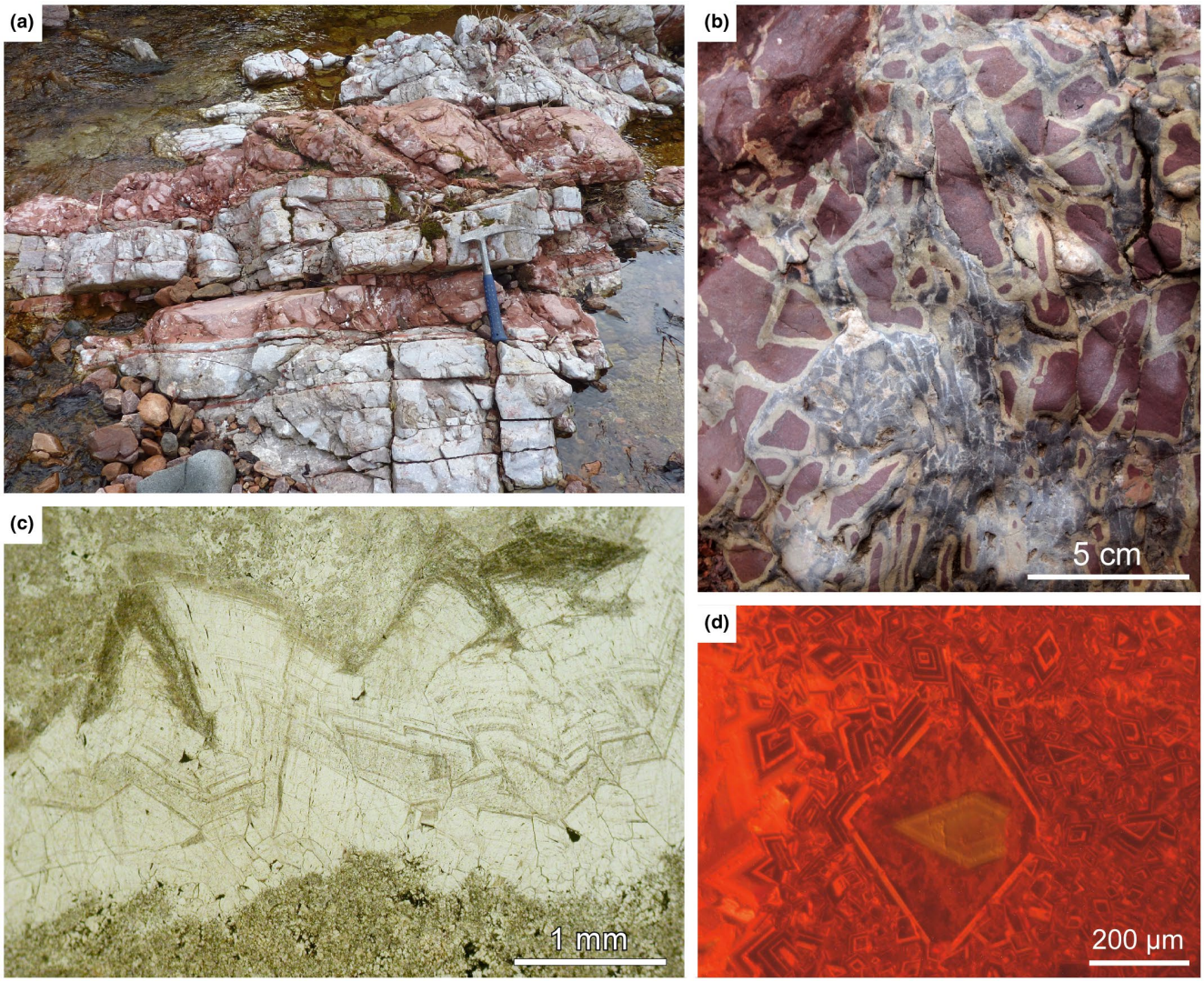

FIGURE 7 Sostegno sector. (a) Dm-thick, bed-parallel fissures in the uppermost part of the SSD, filled with brick-red, finely dolomitized sediments. Hammer for scale is about 30 cm long. (b) Subvertical belt of irregularly shaped cavities within the brick-red sediment infilling the fissures of Figure 7a. The cavities are cemented by a white dolomite cement. A progressive bleaching of the red sediment, from yellowish to grey, occurs approaching the dolomite-filled cavities formerly corresponding to fluid conduits. (c) Photomicrograph of mm-large saddle dolomite crystals cementing the voids of Figure 7b (transmitted, plane polarized light). Note the curved crystal faces. (d) CL image of the dolomitized red sediment infilling the fissures of Figure 7a. Note the occurrence of a sand-sized grain with a detrital greenish core and a syntaxial overgrowth with non-luminescent to orange-red thin zones, which may be easily correlated with the dolomite cements of the Monte Fenera sector breccias (Figure 3d,f)

values of −4.3‰, −6.9‰ and −8.3‰. Two samples of dolomite cements filling Type 1 veins show a $\delta^{18}O$ of −6.9‰ and −8.4‰, whereas two samples of calcite cement filling Type 1 veins show $\delta^{18}O$ values of −13.7‰ and −10.6‰. For one sample of dolomite cement, showing a $\delta^{18}O$ of −9.1‰, petrographic and textural relationships did not allow distinguishing if it represents the filling of a Type 1 or Type 2 vein. All samples show positive $\delta^{13}C$ values, ranging from +0.3‰ to +2.7‰, with the exception of sample MD 1622 with a value of −4.5‰.

Clumped isotope results are shown in Figure 13 and Table 1 (average temperatures and relative uncertainties at 95% confidence level; full data are reported in File S2). In the Monte Fenera–Sostegno area, clumped isotope data for both DOL2 and DOL3 cements indicate temperatures between 80 and 110°C, in good agreement with homogenization temperatures obtained from fluid inclusions from DOL2 cements in the very same samples. Samples of fine-grained SSD, apparently barren of dolomite veins and unaffected by recrystallization, showed clumped isotope temperatures of 48 ± 14°C (SQ1a) and 66 ± 11°C (ANT11). A sample of dolomitized sediments from neptunian dykes at the top of SSD at Sostegno (SO7a) gave a clumped isotope temperature of 49 ± 15°C.

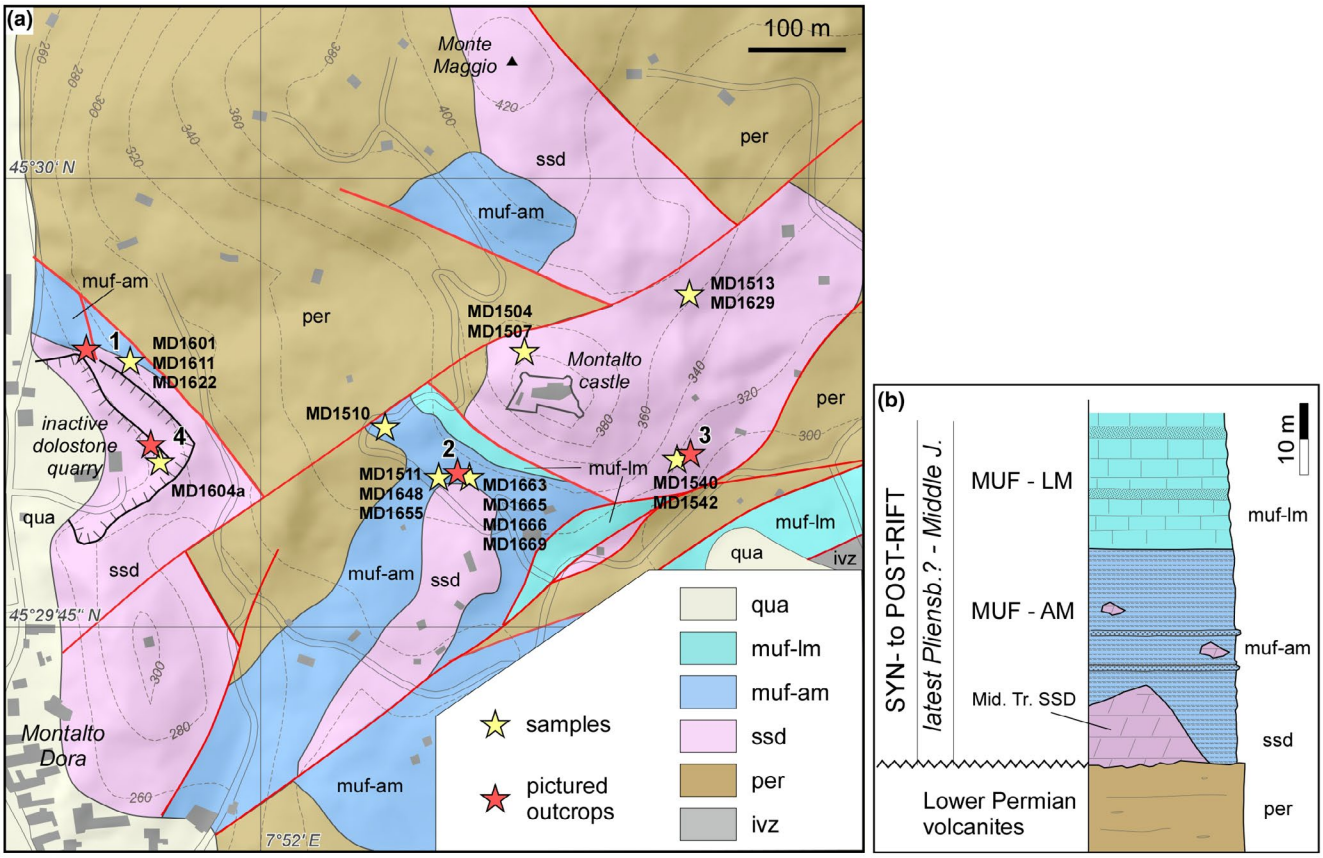

FIGURE 8 (a) Geological scheme of the Montalto Dora sector based on original field surveys. The collection sites of the samples (yellow stars) and the position of the most significant outcrops (red stars) are shown. Legend: qua, Quaternary deposits; muf-lm, Muriaglio Formation, Limestone Member; muf-am, Muriaglio Formation, Arenaceous Member; ssd, San Salvatore Dolostone; per, Permian volcanic and volcanoclastic rocks; ivz, Ivrea–Verbano Zone. (b) Simplified log of the Montalto Dora stratigraphic succession on the SW slope of the Montalto castle hill (i.e. corresponding to outcrop 2 in (a)

In the Montalto Dora sector, clumped isotope temperatures range from around 90 to 350°C, reflecting partial-to-total alteration of the original clumped isotope signatures during alpine metamorphism through recrystallization and/or ^{13}C–^{18}O bond reordering (Stolper & Eiler, 2015). Thus, the temperatures of these samples are not representative of the original precipitation temperature.

5.3 | U/Pb dating

In situ U–Pb isotope analyses were performed on several SSD dolostones, on SSD recrystallized clasts occurring in the Muriaglio Formation and in carbonate cements filling veins and cavities (see File S3 and File S4). These cements, however, could not be dated neither in the Fenera–Sostegno nor in the Montalto Dora area due to very low uranium contents determined in preliminary assays.

In the Monte Fenera–Sostegno sector, two samples of finely crystalline SSD from Cava Antoniotti locality (ANT8, FE2N) and one sample of finely crystalline SSD clasts from the basal part of the overlying SQS (SB5) yielded U/Pb ages, which are in the range of the biostratigraphic age of the SSD (late Anisian-Ladinian; Berra et al., 2009) (Figure 14). In the Montalto Dora sector, three samples of medium-to-coarse crystalline SSD dolostone clasts occurring in the Muriaglio Formation gave radiometric ages spanning the latest Triassic–late Early Jurassic (Figure 15): in particular, one sample yielded a Rhaetian–Sinemurian age (MD1513, 199.2 ± 7.4 Ma) and two a late Pliensbachian–Toarcian age (MD1540, 182.1 ± 5.7 Ma; MD1663 179.6 ± 5.3 Ma). The fine-grained matrix of the samples MD1513 and MD 1663 gave ages much younger than the clasts (MD1513_matrix: 72.7 ± 5.6 Ma; MD1663_matrix: 75 ± 25 Ma). Such ages reflect a partial reopening of the U/Pb system during the Alpine evolution that selectively affected only the fine-grained matrix and left the U/Pb signal of the coarse-crystalline dolomite clasts unaltered. Also a sample of fine-grained SSD dolostone gave a similar young age (MD1507b: 65 ± 16 Ma), which is attributed to a partial resetting of the U/Pb system. The ages of these last three samples have, thus, not been plotted in Figure 15.

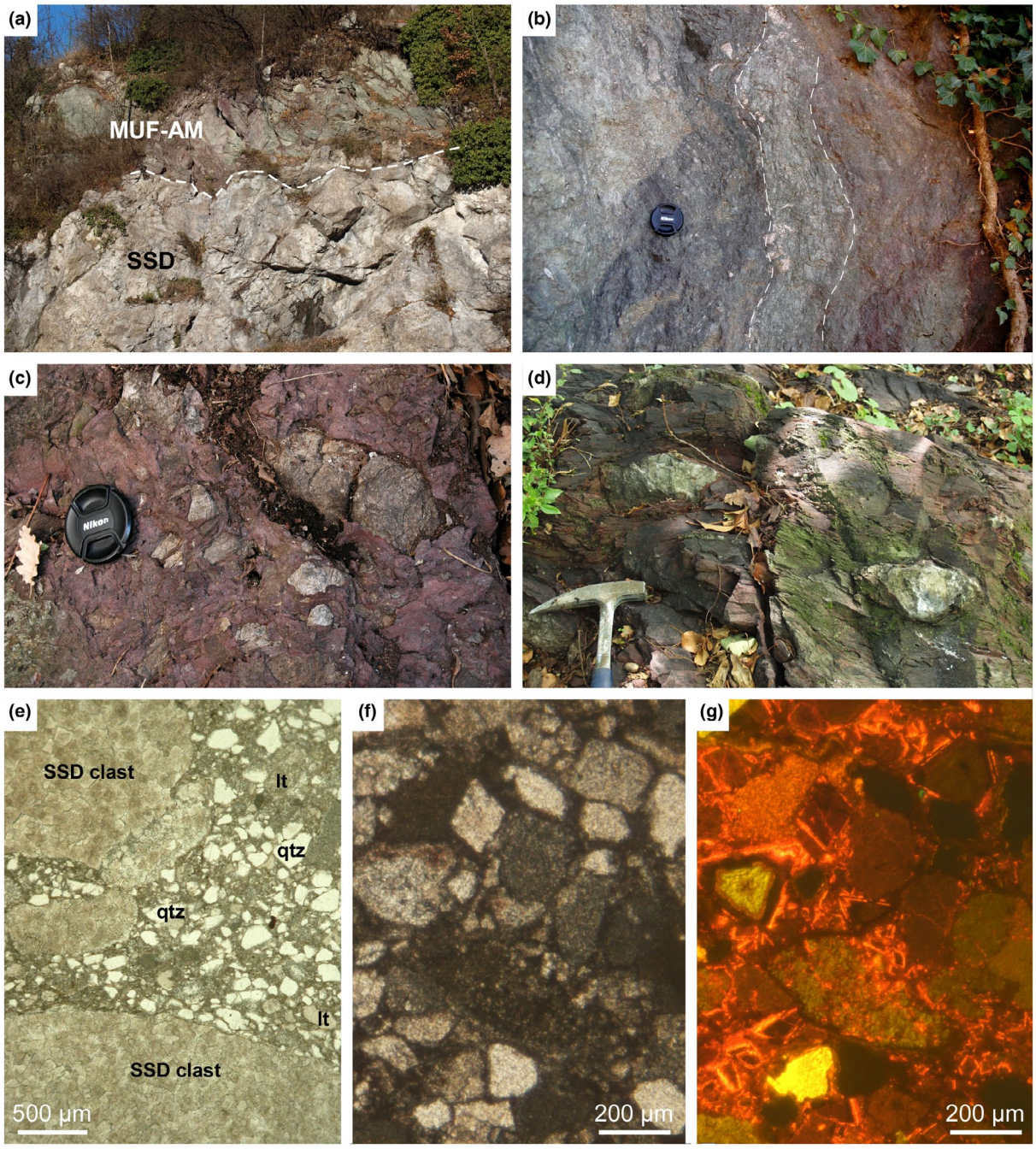

FIGURE 9 Montalto Dora sector. (a) Stratigraphic boundary between the San Salvatore dolostone (SSD) and the overlying Muriaglio formation, Arenaceous Member (MUF-AM), well exposed in the outcrop 1 of Figure 8a. Bedding in the MUF-AM dips to the right, whereas it is not clearly recognizable in the SSD. (b) Decimetre-thick beds of reddish and greenish interbedded coarse sandstones and breccias at the base of the MUF-AM. Younging is to the left. Outcrop 1 in Figure 8a. Lens cap for scale is about 5 cm large. (c and d) MUF-AM: reddish shale with cm- to dm-sized light-coloured SSD clasts in the outcrop 2 in Figure 8a. Lens cap and hammer head for scale are about 5 and 18 cm respectively. (e) MUF-AM thin section (transmitted, plane polarized light), showing mm-sized clasts of coarsely crystalline SSD in a sandy matrix with visible quartz (qtz) and lithic grains (lt). Sample MD1611 (see location in Figure 8a). (f and g) Detail of the MUF-AM (f, transmitted, plane polarized light; b, cathodoluminescence). Note that the SSD grains do not show the same CL colours: both dull-brown and greenish grains occur. Sample MD1601 (see location in Figure 8a)

5.4 | Strontium isotopes

Five samples were measured for $^{87}Sr/^{86}Sr$ values (Table 1, Figure 16). Sample ANT 11, a fine crystalline SSD from Monte Fenera, shows a $^{87}Sr/^{86}Sr$ value of 0.708045 ± 0.00012. Coarse-grained dolomite cements from Monte Fenera (ANT 13; DOL2 cavity cement within SSD) and Sostegno (SO 7b; DOL2 cavity cement within fissure-infilling red sediment) show

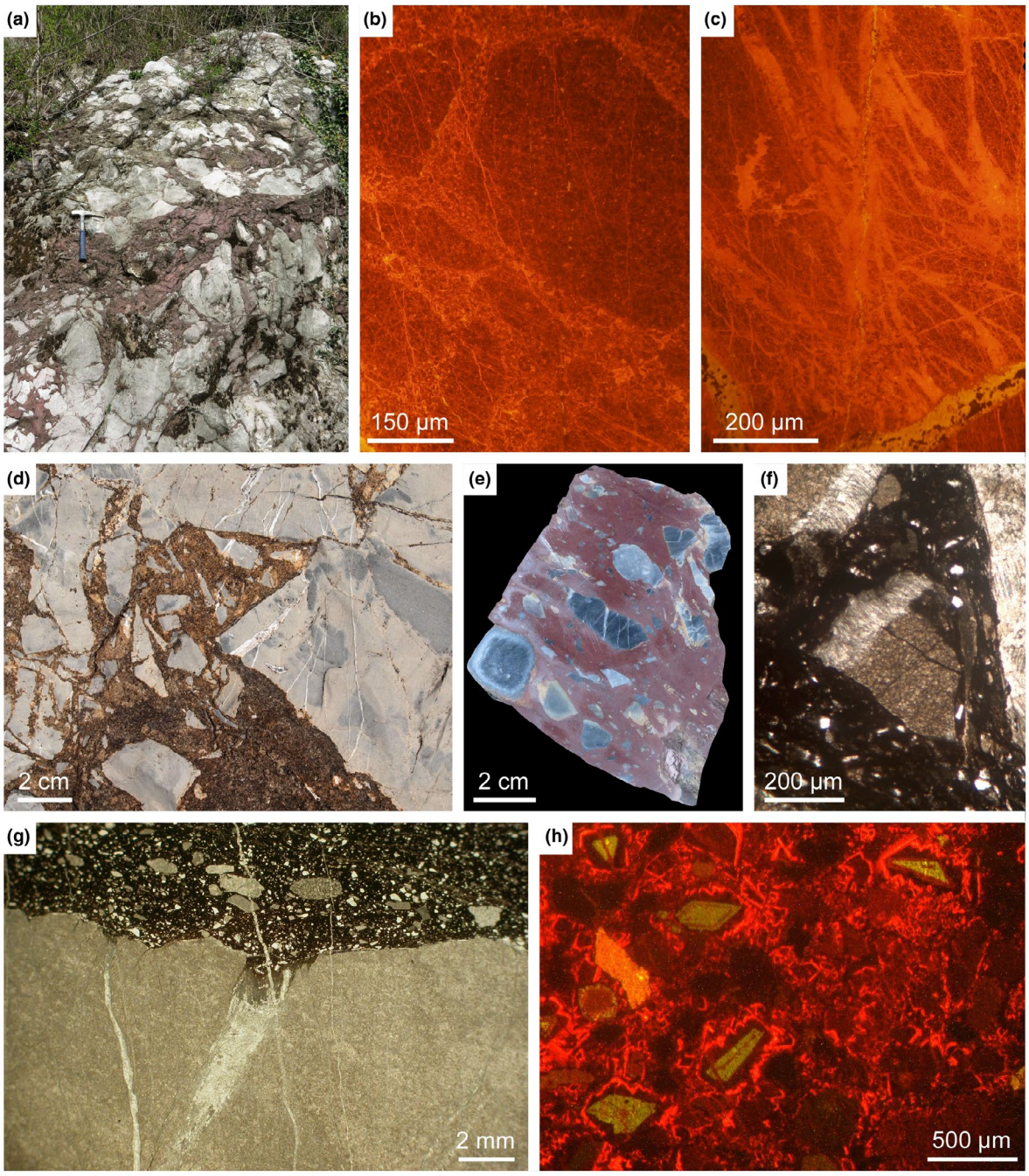

FIGURE 10 Montalto Dora sector. (a) Complex network of neptunian dykes, centimetre- to metre-wide, filled with matrix- or clast-supported breccias, occurring within the uppermost part of the SSD. The reddish matrix is composed of MUF-AM sediments. Outcrop 3 in Figure 8a–c) Cathodoluminescence images of SSD clasts in the MUF-AM, crossed by swarms of dolomite veinlets, a few microns to tens of microns thick, showing a reddish orange CL colour (b). Locally, cataclastic fabrics also occur (c). Note the occurrence of some larger veins cemented by quartz and calcite (non-luminescent and bright yellow, respectively), clearly cross cutting the veinlets. Sample MD1542 (see location in Figure 8a). (d) Dyke infilling, showing cm-sized SSD clasts crossed by millimetre-wide veins abruptly stopping at the boundary of the clasts with the MUF-AM matrix. Outcrop 4 in Figure 8a. (e) Polished sample of MUF-AM. Note the occurrence of mm-large veins confined within the clasts, and thinner veins cross cutting both clasts and matrix. Sample MD1669 (see location in Figure 8a). (f) Photomicrograph (transmitted, plane polarized light) of the MUF-AM, showing a clast composed of a SSD dolostone and a portion of a Type 1 vein at its edge. Sample MD1540 (see location in Figure 8a). (g) Detail of sample MD1669 (Figure 10f) in thin section (transmitted, plane polarized light). The larger vein (Type 1) in the middle of the picture was opened and cemented in the SSD before erosion and deposition as a clast in the MUF-AM, as clearly documented by the facts that it stops at the edge of the clast and that it is differentially eroded with respect to the edges of the clast. Thinner and younger veins occur, cross cutting both the Type 1 vein and the matrix. (h) Cathodoluminescence microphotograph of sand-sized dolomite grains in the MUF-AM. Note the occurrence of greenish irregular cores, overgrown by a syntaxial rim with non-luminescent to orange-red thin zones. See Figures 7d and 9g for comparison. Sample MD1601 (see location in Figure 8a)

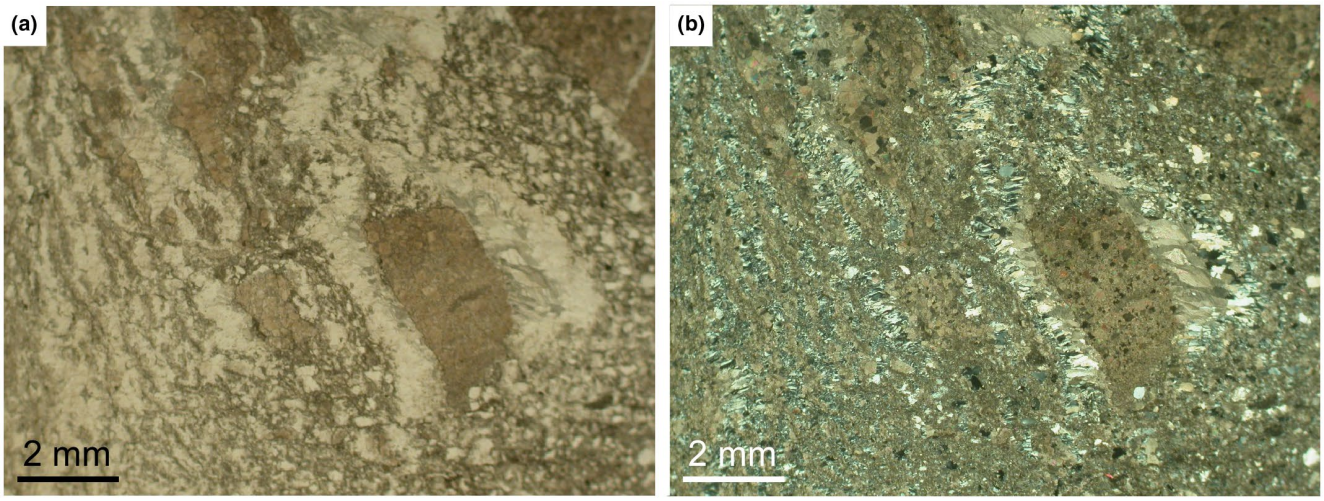

FIGURE 11 Submillimetre- to millimetre-wide, quartz–calcite filled Type 2 veins in the sandy matrix of a matrix-supported breccia of the MUF-AM under the microscope (a: transmitted, plane polarized light; b: transmitted, crossed polarized light). Note that the veins are discontinuous and show irregular margins and enlarged at the coarse sand grain outer boundary. Sample MD1510 (see location in Figure 8a)

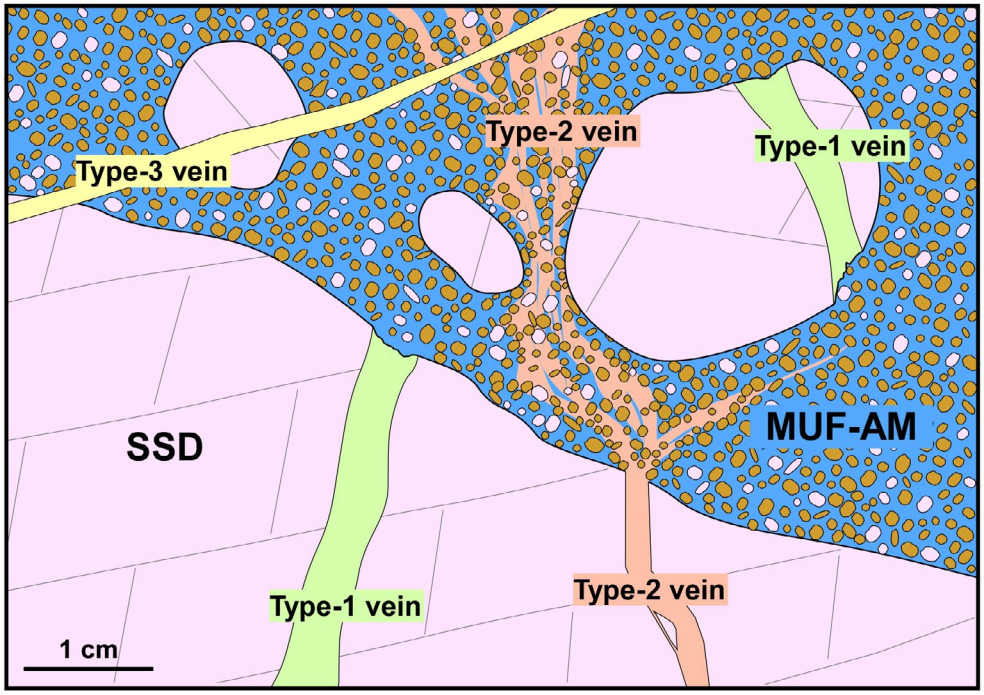

FIGURE 12 Scheme of the observed relationships between the three recognized vein generations and the host rocks in the Montalto Dora sector (San Salvatore Dolostone, SSD, and Muriaglio Formation, MUF-AM)

values of 0.707511 ± 0.000008 and 0.712982 ± 0.000007 respectively. Samples MD 1511 (coarse crystalline dolomite cement of Type 1 vein within a SSD block in the Muriaglio Fm.; Montalto Dora) and MD 1,540 (coarse crystalline SSD dolostone clast from Muriaglio Fm., Montalto Dora) show values of 0.709110 ± 0.000012 and 0.709695 ± 0.000006 respectively.

6 | DATA INTERPRETATION

The stratigraphy and geometry of sedimentary bodies document a different architecture of the Triassic-to-Middle Jurassic succession in the two study areas reflecting their distinct positions on the Adriatic continental margin. Petrographic,

TABLE 1 Summary of analytical results for Monte Fenera–Sostegno and Montalto Dora samples

Sample (dolomites)	Locality	Description	$\delta^{13}C$ (‰VPDB)	$\delta^{18}O$ (‰VPDB)	Fluid inclusion homogenization temperature (Th)			Sr isotopes		Clumped isotopes			
					Th min. (°C)	Th max. (°C)	Th average (°C)	$^{87}Sr/^{86}Sr$	*SE* (abs)	Δ47 CDES (@70°C)	Δ47 *SD*	*T* average (°C)	Uncertainty (95% CL)
FE2a	Monte Fenera	DOL2 cavity cement (in SSD)	1.81	−9.46	87.4	105.9	96.9	—	—	0.453	0.027	103	14
FE2b	Monte Fenera	Dolomitic internal sediments of cavity (in SSD)	2.26	−7.60	—	—	—	—	—			—	—
FE2c	Monte Fenera	DOL3 vein cement (in SSD)	1.44	−10.30	—	—	—	—	—	0.442	0.026	109	14
ANT8	Monte Fenera	DOL2 breccia cement (in SSD)	1.22	−9.83	103.1	114.9	109.9	—	—	0.482	0.022	85	10
ANT11	Monte Fenera	Fine crystalline SSD dolostone	1.59	−2.26	—	—	—	0.708045	0.000012	0.521	0.028	66	11
ANT13	Monte Fenera	DOL2 cavity cement (in SSD)	—	—	—	—	—	0.707511	0.000008			—	—
ARA3	Monte Fenera	DOL2 cavity cement (in SSD)	1.90	−8.53	140.0	239.9	188.7	—	—	0.441	0.045	112	19
ARA3b	Monte Fenera	Dolomitic internal sediments of cavity (in SSD)	2.65	−1.62	—	—	—	—	—			—	—
SQ1a	Monte Fenera	Fine crystalline SSD dolostone	2.04	−4.33	—	—	—	—	—	0.563	0.023	48	14
SQ1b	Monte Fenera	DOL2 vein cement (in SSD)	1.75	−10.03	—	—	—	—	—	0.491	0.033	81	12
SQ6−7	Monte Fenera	DOL2 cavity cement (in SQS)	2.30	−9.98	87.5	112.8	98.4	—	—	0.465	0.017	94	9
SO1a	Sostegno	Fine crystalline SSD dolostone	0.97	−3.00	—	—	—	—	—			—	—
SO1b	Sostegno	Dolomitized red sediment in dyke	3.72	−6.63	—	—	—	—	—			—	—
SO7a	Sostegno	Dolomitized red sediment in dyke	3.11	−4.07	—	—	—	—	—	0.561	0.023	49	15
SO7b	Sostegno	DOL2 cavity cement (within red sediments in dyke)	2.37	−9.51	—	—	—	0.712982	0.000007	0.440	0.021	110	36
SO7c	Sostegno	Dolomitic internal sediments of cavity (within red sediments in dyke)	2.47	−8.68	—	—	—	—	—			—	—
SO7d	Sostegno	Dolomitized SQS matrix in dyke (bleached halo)	2.99	−4.71	—	—	—	—	—			—	—
MD1504	Montalto Dora	Coarse crystalline SSD dolostone (clast in MUF)	0.99	−8.34	—	—	—	—	—	0.318	0.032	236	33
MD1507a	Montalto Dora	Type 1 vein dolomite cement	1.24	−6.89	100.1	130.6	117.0	—	—	0.267	0.034	351	78
MD1507b	Montalto Dora	Fine crystalline SSD dolostone	1.47	−5.06	—	—	—	—	—	0.473	0.016	90	7

(Continues)

TABLE 1 (Continued)

Sample (dolomites)	Locality	Description	$\delta^{13}C$ (‰VPDB)	$\delta^{18}O$ (‰VPDB)	Fluid inclusion homogenization temperature (Th)			Sr isotopes		Clumped isotopes			
					Th min. (°C)	Th max. (°C)	Th average (°C)	$^{87}Sr/^{86}Sr$	*SE* (abs)	Δ47 CDES (@70°C)	Δ47 *SD*	*T* average (°C)	Uncertainty (95% CL)
MD1511	Montalto Dora	Type 1 vein dolomite cement	—	—	—	—	—	0.709110	0.000012			—	—
MD1540	Montalto Dora	Coarse crystalline SSD dolostone (clast in MUF)	—	—	—	—	—	0.709695	0.000006			—	—
MD1604a	Montalto Dora	1) Fine crystalline SSD dolostone	2.84	−4.93	—	—	—	—	—	0.391	0.022	148	14
		2) Type 1 vein dolomite cement	1.58	−8.42	98.1	138.6	120.6	—	—	0.449	0.027	105	13
		3) Type 1 vein quartz cement	—	—	92.8	119.2	105.4	—	—			—	—
MD1622	Montalto Dora	Coarse crystalline SSD dolostone (clast in MUF)	−4.54	−4.30						0.366	0.032	175	27
MD1629	Montalto Dora	Type 2 vein quartz cement	—	—	76.6	109.0	99.0	—	—			—	—
MD1648	Montalto Dora	Type 1 vein quartz cement	—	—	106.3	124.6	114.8	—	—			—	—
MD1655	Montalto Dora	Type 1 vein dolomite cement	1.91	−9.06	—	—	—	—	—	0.265	0.022	343	47
MD1665	Montalto Dora	Coarse crystalline SSD dolostone (clast in MUF)	1.52	−6.30	—	—	—	—	—	0.352	0.035	191	38

Sample (calcites)	Locality	Description	$\delta^{13}C$ (‰VPDB)	$\delta^{18}O$ (‰VPDB)	Fluid inclusion homogenization temperature (Th)			Sr isotopes		Clumped isotopes			
					Th min. (°C)	Th max. (°C)	Th average (°C)	$^{87}Sr/^{86}Sr$	*SE* (abs)	∇47 CDES (@25°C)	Δ47 *SD*	*T* average (°C)	Uncertainty (95% CL)
MD1666	Montalto Dora	Type 1 vein calcite cement	1.64	−10.48	—	—	—	—	—	0.457	0.04	123	30
MD1669	Montalto Dora	Type 1 vein calcite cement	0.33	−13.71	—	—	—	—	—	0.372	0.04	203	34

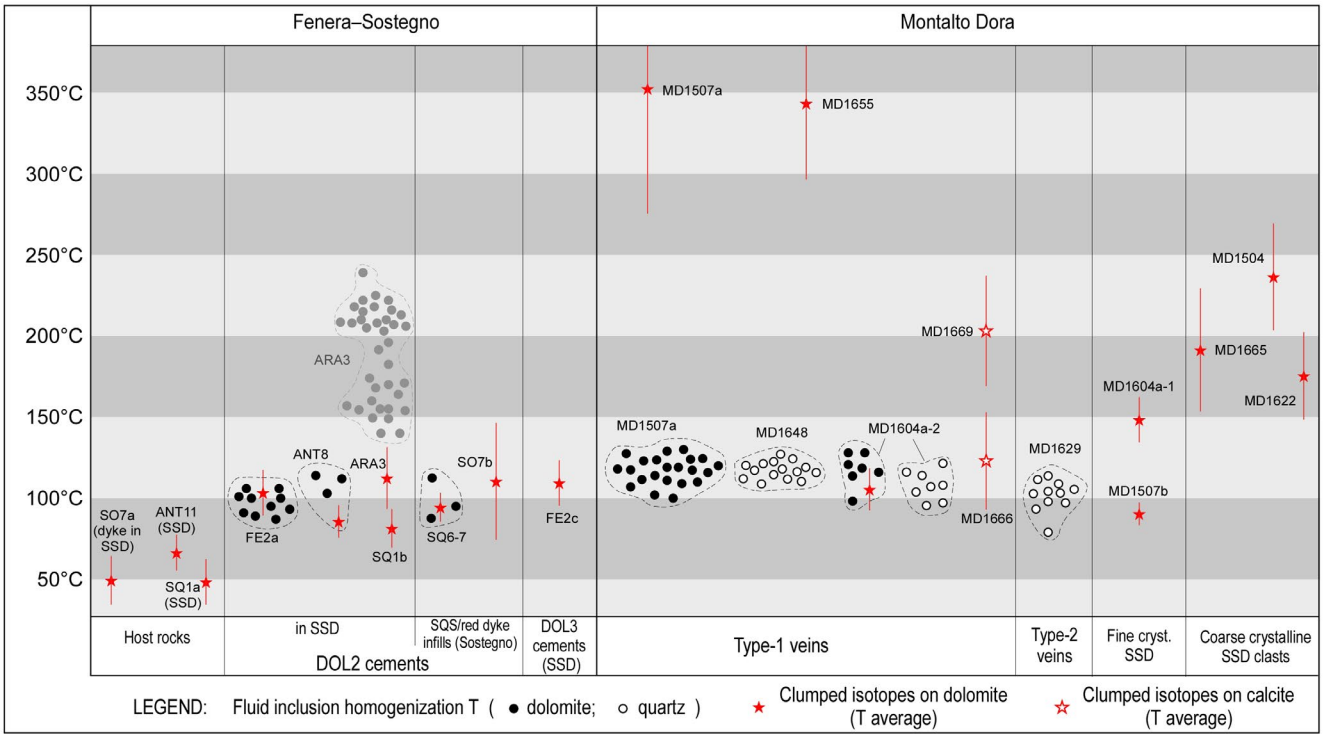

FIGURE 13 Fluid inclusion microthermometry (homogenization temperatures) and clumped isotopes data (average temperatures horizontal bars represent uncertainties at 95% confidence level). See locations of the samples in Figures 2 and 8a. Fluid inclusion data for ARA3 are shown in grey since they are thought to have undergone post-entrapment modifications (see text). Clumped isotope temperatures in the Montalto area have been affected by alpine metamorphism

geochemical and geochronological data on diagenetic products provide information on the circulation of hydrothermal fluids, and on their composition and flow pathways. Given the differences between the two study areas, they will be first discussed separately and then in the frame of the rifting evolution of the western part of the Adriatic continental palaeomargin.

6.1 | Monte Fenera–Sostegno sector

6.1.1 | Stratigraphic and petrographic evidence for fluid circulation

As illustrated in previous studies (Berra et al., 2009; Fantoni et al., 2003), the Permian-to-Toarcian stratigraphic succession is strongly condensed because of prolonged sedimentation hiatuses corresponding to the Early Triassic and to the Late Triassic–Early Pliensbachian, although no angular unconformities are recognizable. This stratigraphic succession, with more gaps than record, is related to a structurally high position of this sector, that is, a position characterized by prevailing subaerial conditions without deposition and erosion. In the Monte Fenera–Sostegno succession, different structures document fluid circulation within a framework of fissures and cavities of secondary origin in the SSD. At Monte Fenera, breccias, either concordant or discordant with respect to bedding, show features pointing to a hydrofracturing process and are cemented by coarsely crystalline, commonly saddle, dolomite. At Sostegno, centimetre-sized cavities, cemented by coarse saddle dolomite, occur within the infillings of large neptunian dykes in the uppermost part of the SSD. In addition, thin dolomite-cemented veins perpendicular to bedding cross both the SSD and the SQS. The latter veins show a sudden change in morphology (from straight fractures in SSD to irregularly shaped cavities in SQS, see Section 4.1. Figure 5a–c), which clearly documents that the lower part of the SQS had to be only partially consolidated when the veins opened. In turn, this can be related to a limited compaction and, thus, to a thin overburden. A further support to this interpretation is provided by the occurrence of fine-grained red internal sediments associated with dolomite cements in veins and cavities in the SSD. This occurrence testifies that both the veins and the cavities were opened in a shallow burial setting still in connection with the seafloor so that the reddish fine-grained matrix of the overlying unconsolidated SQS could infiltrate in the fractures. The complexity of the dolomite cements, in particular in the breccias, well evidenced by cathodoluminescence petrography (Figure 3b–f), documents the polyphase character of their diagenetic evolution, during which episodes of dolomite and calcite cements precipitation, sediment infiltration and calcite dissolution alternated (Figure 4). On the basis of

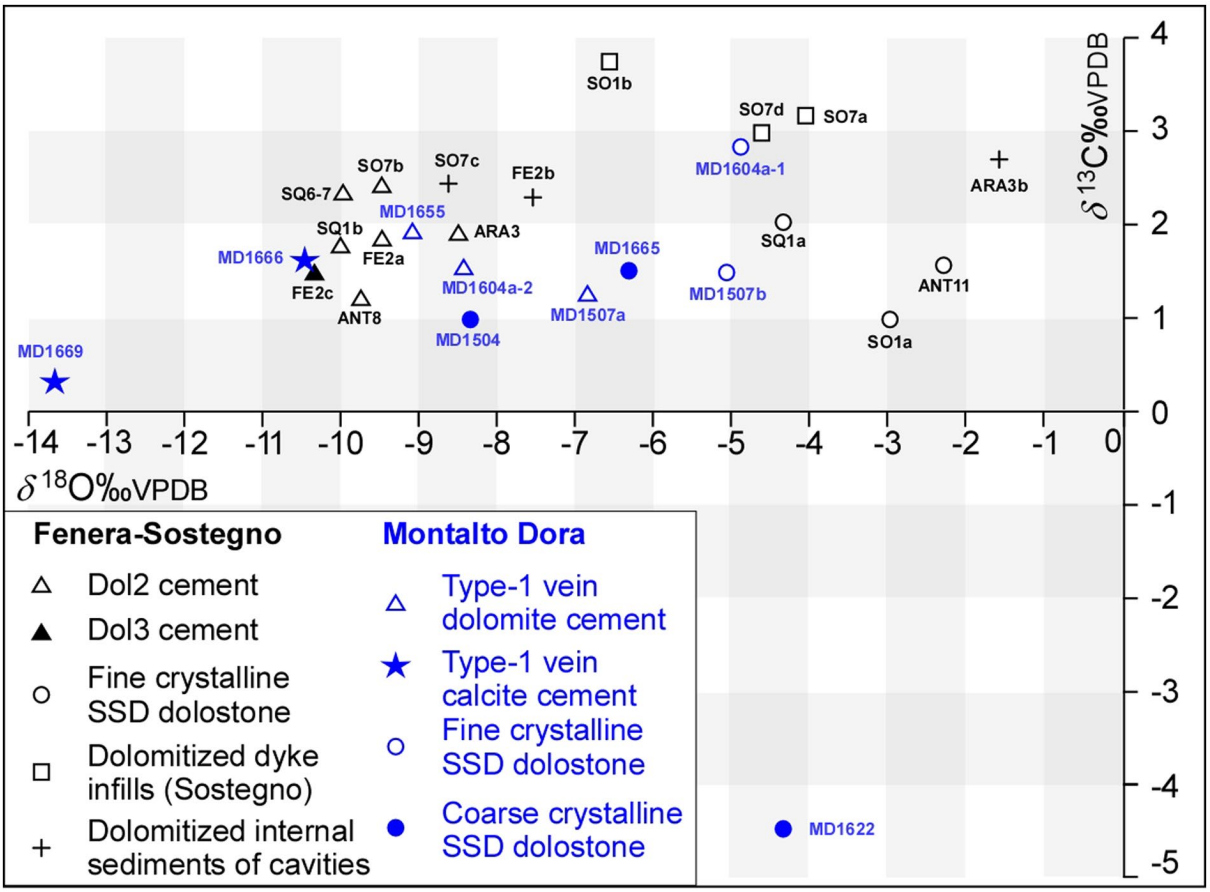

FIGURE 14 $\delta^{18}O$ versus $\delta^{13}C$ cross-plot for dolomite and calcite cements, SSD dolostones, dolomitized SQS matrix and dolomitized sediments in both Monte Fenera–Sostegno and Montalto Dora areas (values relative to VPDB standard)

these considerations, it may be inferred that an upward flux of overpressured fluids crossed subvertically the Middle Triassic-to-Pliensbachian succession shortly after the beginning of the SQS deposition. This flux produced different features, depending on the rheology of the cross-cut lithologies: subvertical, sharp-edged cracks or bedding-parallel dilation breccias developed along less resistant horizons (e.g. supratidal laminated sediments) in fully lithified rocks (SSD); subvertical, but irregularly shaped, fissures in uncemented sandstones (SQS); and very irregular rounded cavities in uncemented fine-grained fillings of neptunian dykes.

6.1.2 | Fluid temperature, hydrothermal nature, isotopic composition and origin

Temperatures of fluids during dolomite precipitation, as revealed by fluid inclusion microthermometry and clumped isotopes, were between 80 and 120°C. Only in one sample (ARA3; see Figure 13), homogenization temperatures obtained from fluid inclusions within coarse crystalline dolomite cements were considerably higher and dispersed over a range of about 100° (140–239°C). On the contrary, clumped isotope measurements on the same dolomite cements indicate a temperature of 112 ± 19°C, which is in the range of homogenization temperatures obtained from other DOL2 cements of the Monte Fenera–Sostegno sector. For this reason, we consider the fluid inclusion homogenization temperatures obtained on ARA3 dolomite cement as not reliable, possibly due to cryptic (i.e. not evident under the microscope) post-entrapment modifications experienced by these fluid inclusions. Given the very shallow burial setting discussed above (Section 6.1.1), such fluids were considerably hotter than host rocks and, thus, they can be properly considered as hydrothermal fluids (sensu Davies & Smith, 2006; Machel, 2004; Machel & Lonnee, 2002).

The isotopic composition of dolomite shows slightly positive $\delta^{13}C$ values, varying from +1.0‰ to +3.7‰ VPDB. The $\delta^{13}C$ values overlap with those from Triassic and Jurassic sediments not affected by hydrothermal dolomitization and are in the range of marine carbonates (e.g. Nunn & Price, 2010; Podlaha et al., 1998). This indicates that carbon isotope composition of the dolomite was rock buffered, as is commonly observed in dolomitization processes (e.g. Hoefs, 2018). The $\delta^{18}O$ values are all negative, being more negative for the void-filling dolomite cements.

By combining the $\delta^{18}O$ of DOL2 cements, the fluid inclusion homogenization temperatures (Figure 17a; see also File S5)

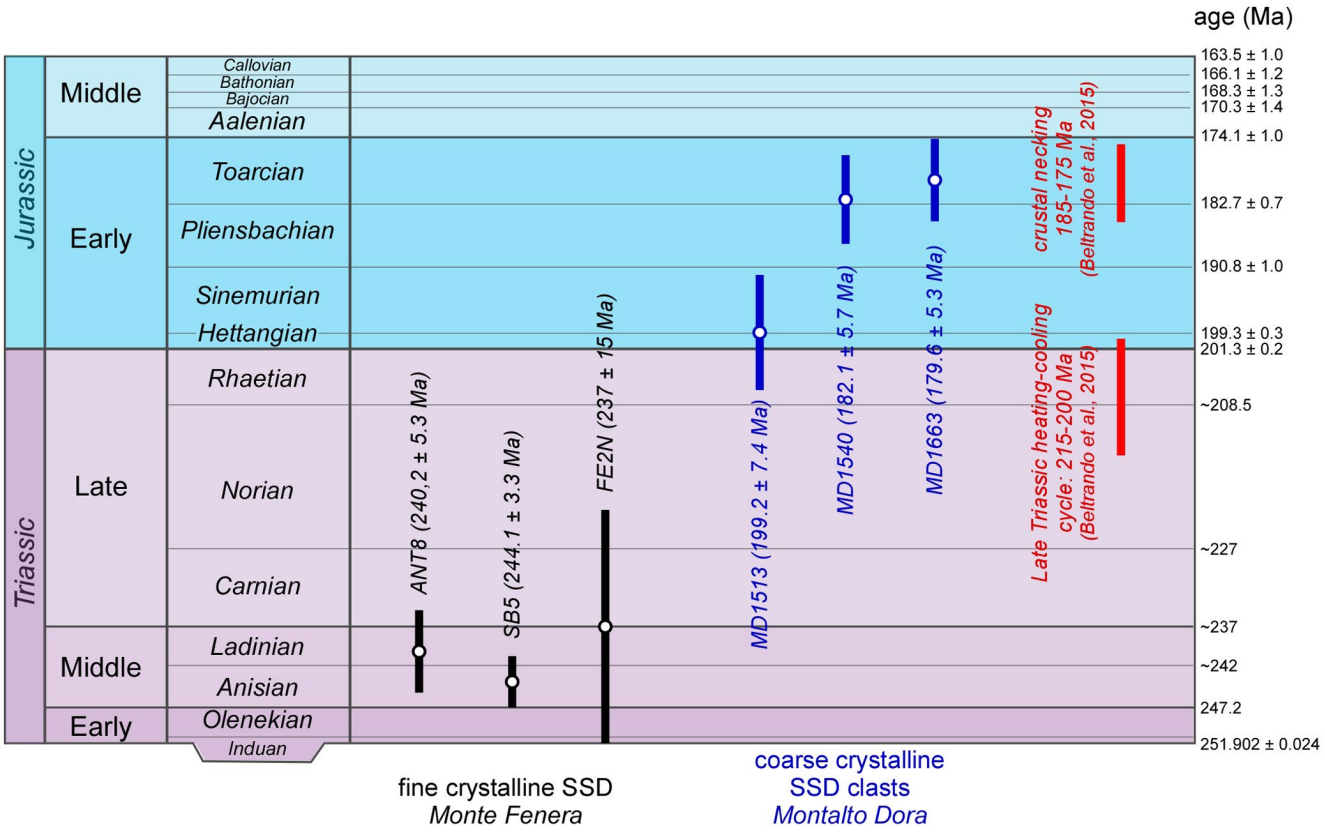

FIGURE 15 Results of U/Pb radiometric datings of samples of non-recrystallized SSD from Monte Fenera area (black bars) and clasts of recrystallized SSD from Montalto Dora (blue bars). The time spans of regional thermal and tectonic events reported in the literature are also indicated (red bars; see discussion in the text). Numerical ages of geochronologic unit boundaries conform to the International Chronostratigraphic Chart, version 2018/08 (Cohen et al., 2013; updated)

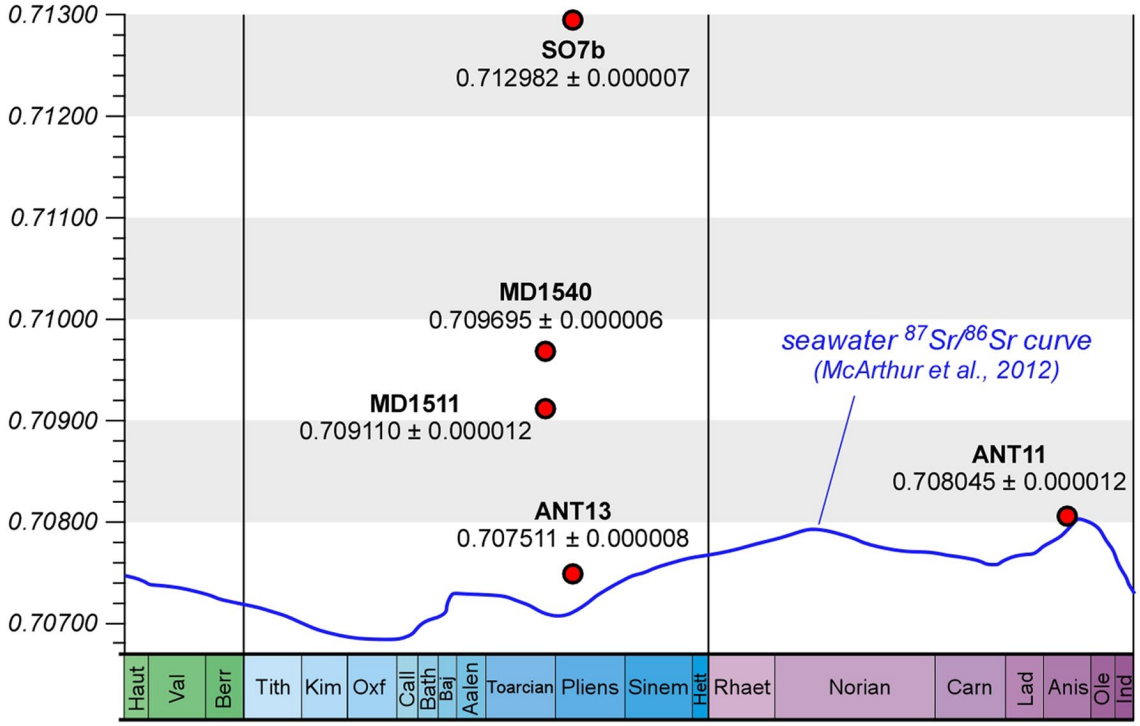

FIGURE 16 $^{87}Sr/^{86}Sr$ values measured on samples from Monte Fenera (ANT11, ANT13), Sostegno (SO7b) and Montalto Dora (MD1511, MD1540), plotted together with the seawater $^{87}Sr/^{86}Sr$ curve of McArthur et al. (2012)

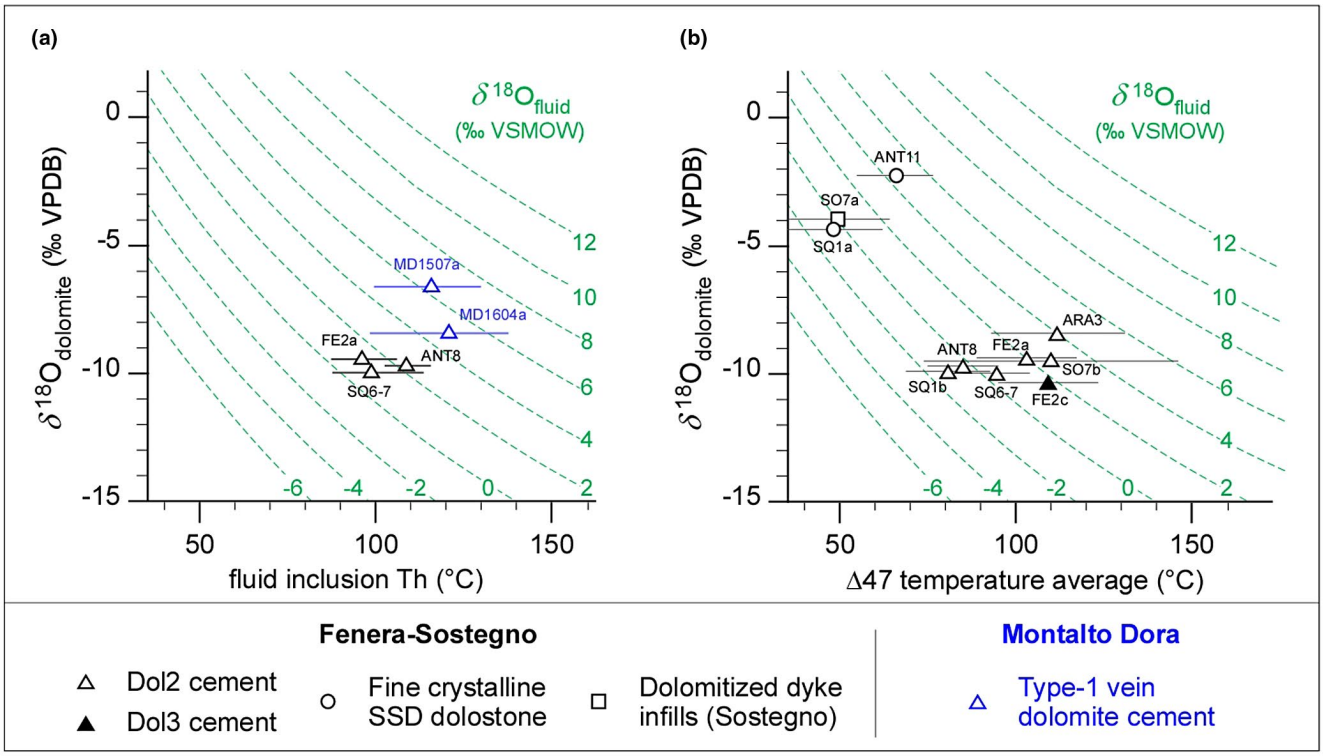

FIGURE 17 Cross-plots between δ^{18}Odolomite and fluid inclusion Th (a) and between δ^{18}odolomite and clumped isotope average temperatures (b; horizontal bars represent uncertainties at 95% confidence level). Isotopic composition of fluids in equilibrium with the dolomite are calculated with the fractionation equation of Müller et al. (2019). In (a), the symbols are centred on the average Th, whereas the horizontal bars represent the range of measured Th values (Thmin–Thmax)

and the clumped isotope temperatures (Figure 17b; see also File S2) in the equation of Müller et al. (2019), δ^{18}O values of dolomitizing fluids ranging from around −1‰ to +4‰ VSMOW (Vienna Standard Mean Ocean Water) have been obtained. The more positive values could point to evaporitic or basinal brines, which are commonly indicated as possible sources of dolomitizing, ^{18}O-enriched fluids in hydrothermal systems (Davies & Smith, 2006; Lapponi et al., 2014; López-Horgue et al., 2010; Shah et al., 2012; Shelton et al., 2019). However, the absence of evaporites in the Monte Fenera–Sostegno succession, and its limited thickness, and the open marine depositional environment of the late Pliensbachian (the age of dolomite precipitation) definitely rule out basinal and evaporitic brines as sources for ^{18}O-enriched fluids. Therefore, the only possible source for dolomitizing fluids is seawater, whose original composition could have been slightly enriched in ^{18}O in the hydrothermal system by water–rock interactions with crystalline and volcanic/volcanosedimentary rocks, for example, by hydrolytic alteration of ^{18}O-rich anhydrous silicates such as feldspars (Clayton et al., 1966; Hitchon & Friedman, 1969; Land & Prezbindowski, 1981; Pirajno, 2009). This source is also consistent with the Sr isotopes. A finely crystalline SSD dolostone has an ^{87}Sr/^{86}Sr ratio consistent with the Anisian seawater, that is, the seawater at the age of early diagenetic dolomitization. On the contrary, two dolomite cements show ^{87}Sr/^{86}Sr ratios significantly higher than expected for late Pliensbachian seawater. Such enrichment in radiogenic Sr isotope demonstrates a primary crustal contribution and, thus, supports a circulation of hydrothermal fluids through crystalline and volcanic/volcanosedimentary rocks. Comparable Sr isotope values have indeed been reported in the Permian magmatic rocks, which directly underlie the studied succession (Sinigoi et al., 2016).

The lower, slightly negative, δ^{18}O values calculated for the fluids could reflect a minor influence of meteoric waters, in agreement with the tectono-sedimentary setting of the Monte Fenera–Sostegno area in the Pliensbachian. The SQS were deposited on a subaerial erosional surface at the top of Triassic dolostones, in a shallow marine area. Their deposition marks the onset of a major extensional episode, with main normal faults bounding the newly formed basins of Monte Fenera and Sostegno (Beltrando et al., 2015; Berra et al., 2009). Such basins were adjacent to an emerged land which sourced clasts of both Permian volcanic and Triassic dolostones to the basin. Meteoric waters could, thus, also infiltrate the faulted and fractured substrate and mix in various proportions with seawater, possibly influencing the original oxygen isotopic fingerprint.

6.1.3 | Age of hydrothermal circulation

In the Monte Fenera sector, the circulation of hydrothermal fluids is well constrained by the late Pliensbachian age of the

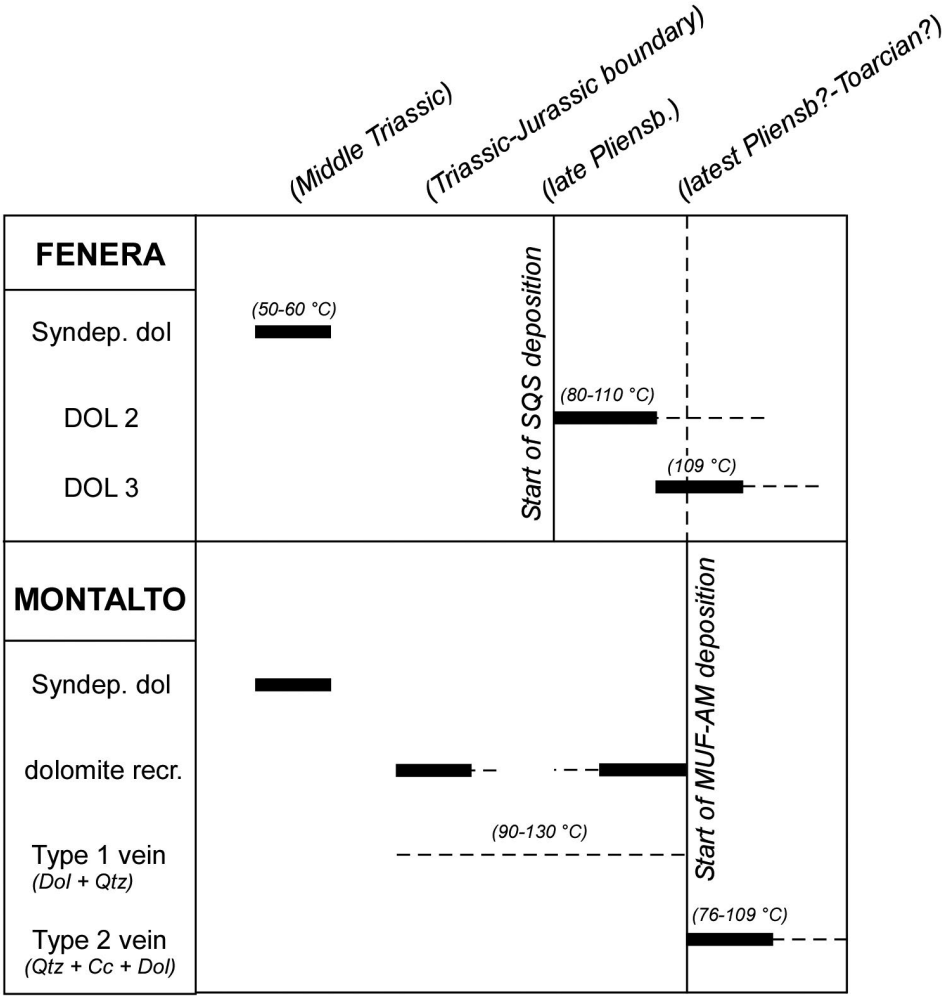

FIGURE 18 Comparative paragenetic sequences for the two study sectors. Depositional events allow chronostratigraphic constraint of diagenetic processes

lower interval of the SQS, and by its relationships with dolomite veins (Figure 18), in spite of the lack of U/Pb dating of the hydrothermal phases. Petrographic evidence shows that the veins opened in semi-consolidated sediments shortly after the deposition of the SQS (see Section 6.1.1). At Sostegno, any biostratigraphic constraints are available. However, within the dyke infillings, the presence of irregularly shaped conduits and cavities cemented by hydrothermal dolomite, and of dolomite overgrowths on detrital monocrystalline dolomite grains (both closely similar to those observed at the base of SQS at Monte Fenera), suggests a common age of dyke infillings and of deposition of the lower part of SQS.

6.2 | Montalto Dora sector

6.2.1 | Stratigraphic evidence for a hyperextended distal margin setting

Despite many lithological affinities with the Mesozoic succession of the Monte Fenera–Sostegno area already reported by Berra et al. (2009), our new field data highlight striking differences in the stratigraphic architecture of the MD sector. In former studies, the present-day geometry of the sedimentary bodies in the MD sector had been attributed uniquely to the effects of the activity of the Internal Canavese Line during Alpine deformation (Ahrendt, 1972; Baggio, 1965; Wozniak, 1977). Because of their local occurrence above the Lower Permian volcanics, part of the Muriaglio Formation sediments were erroneously attributed to the Upper Permian Verrucano Fm. (Baggio, 1965). However, both the observed occurrence of Middle Triassic dolostone clasts and the stratigraphic position, in places above the SSD, definitely rules out such interpretation. Moreover, the local stratigraphic contact of the Muriaglio Formation directly above the Lower Permian volcanics clearly documents that the lateral discontinuity of the SSD was a primary feature, acquired by Middle Triassic sediments during the Early–Middle Jurassic rifting. The composition of the Muriaglio Formation sandstones that include grains of metamorphic rocks and micas, Permian volcanics and Middle Triassic

dolostones indicates that the entire succession, from the Variscan basement to the Triassic platform, was exposed at surface during its sedimentation. In particular, dolostone clasts occur as sand grains, clasts, blocks and as hectometre-sized bodies in the MUF-AMs. The bodies do not appear to be embedded within the Muriaglio Formation sediments, and their basal boundary is never exposed. Recent studies (Beltrando et al., 2015; Decarlis et al., 2017; Ferrando et al., 2004) place the Montalto Dora area between the Fenera–Sostegno necking zone at the east and the hyperextended distal margin preserved in the western termination of the Canavese Zone (Figure 1). According to this scenario, we propose that the hectometre-sized SSD bodies rest directly above the Lower Permian volcanics, or even above the Variscan basement rocks, through the presence of a tectonic, non-stratigraphic, boundary that pre-dates the deposition of the Muriaglio formation. We interpret them as small-sized extensional allochthons occurring above low-angle extensional faults (Figure 19), which started their activity in the Pliensbachian. This rifting phase is clearly distinct from the Hettangian one, which was characterized by diffuse normal faulting and which is well recorded in the proximal part of the Adriatic margin. This interpretation is also supported by the common occurrence of breccias with fabrics suggestive of hydrofracturing related to circulation of overpressured fluids along fault damage zones in the Triassic dolostones, at the base of the allochthons and within the Triassic dolostones. The MUF-AM fine-grained sediments, in which cm- to dm-thick sandstone and breccia beds, are interlayered, document a deposition in the lower part of an irregular slope in a marine environment, where rocks of different units (Variscan basement and Lower Permian volcanics, locally overlained by allochthons of Triassic dolostones) were exposed and sourced coarser sediments.

6.2.2 | Stratigraphic and petrographic evidence for fluid circulation

In such a complex stratigraphic architecture, multiple fluid circulation events followed one another between the Late Triassic and the Middle Jurassic. Some of these preceded the deposition of the Muriaglio Formation and caused the dolomitization and/or silicification of portions of the SSD, in addition to an intense fracturing and opening of veins cemented by dolomite and quartz (Type 1 veins, Figures 12 and 18). Another phase of fluid circulation occurred after the deposition of the MUF-AM, formed the veins filled with quartz, calcite and dolomite (Type 2 veins, Figures 12 and 18) and caused further dolomite precipitation as syntaxial overgrowths around clastic dolomite grains. Both the irregular morphology of the veins and the occurrence of dolomite cement rims over detrital dolomite grains strongly suggest that fluids flowed through the Muriaglio Fm. sediments when they were still highly porous and poorly lithified, that is, shortly after their deposition. This process

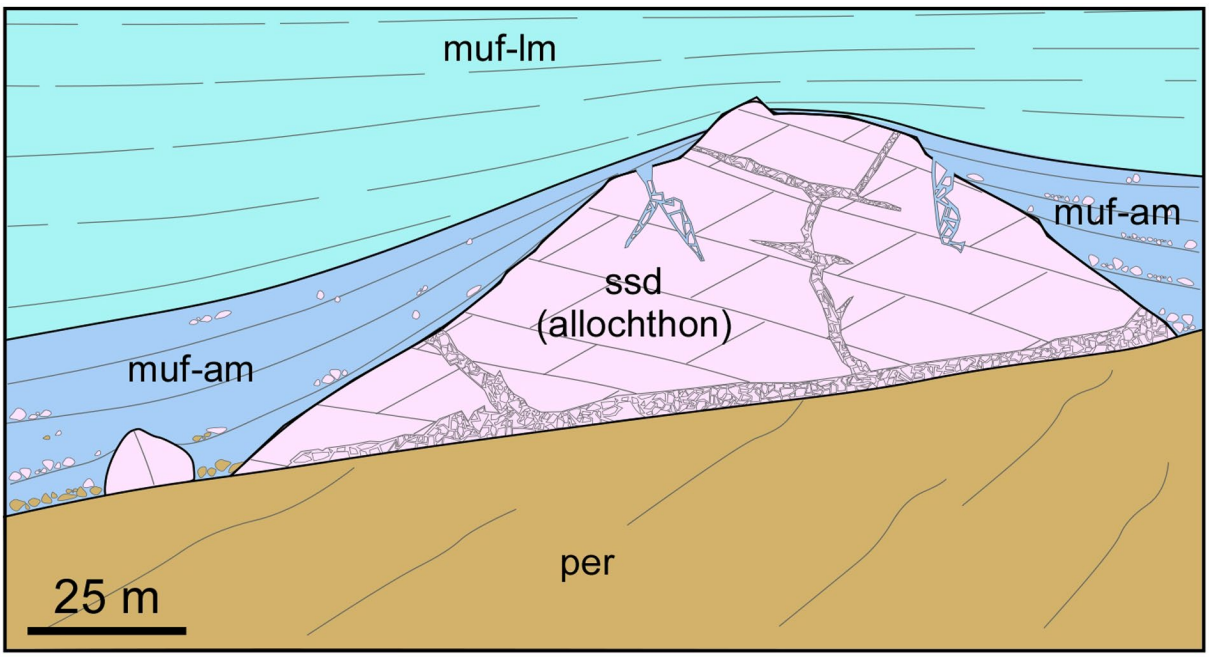

FIGURE 19 Montalto Dora sector (distal margin). Scheme of the inferred stratigraphic relationships between the Middle Triassic San Salvatore Dolostone and the other terms of the stratigraphic succession

is similar to that affecting the SQS in the Monte Fenera–Sostegno sector.

6.2.3 | Fluid temperature, hydrothermal nature, isotopic composition and origin

Fluid inclusions microthermometry data and O, C and Sr stable isotopes values point to temperature and isotopic composition of fluids similar to those of the Monte Fenera–Sostegno sector. Fluid inclusion homogenization temperatures, both from Type 1 and Type 2 quartz and dolomite cements (Figure 12), are strongly consistent and mostly comprised between 90 and 130°C. Considering the shallow depth of cement precipitation, they prove the hydrothermal nature of the fluids. Both $\delta^{13}C$ and $\delta^{18}O$ values from cements and dolostones are in the same range as those from Monte Fenera–Sostegno. Calculation of $\delta^{18}O$ of the parent fluids was made by combining the $\delta^{18}O$ of dolomite cements of Type 1 veins and the fluid inclusion homogenization temperatures (Figure 17a; see also File S5) obtained on the same samples (according to the fractionation equation of Müller et al., 2019). The calculated $\delta^{18}O$ values for parent fluids range from +5‰ to +6‰ VSMOW. As for Monte Fenera–Sostegno, these values document the interaction of seawater with crystalline rocks during their flow through the hydrothermal system. On the contrary, since all the values are markedly positive, the hypothesis of a mixing with meteoric waters (advanced for the Monte Fenera–Sostegno sector, see Section 6.1.2) can be confidently ruled out. Since we could not analyse stable isotopes on carbonate cements of Type 2 veins, the inferred $\delta^{18}O$ values of parent fluids cannot be extended to the younger event of fluid circulation, which followed the beginning of the MUF-AM deposition. However, a seawater origin of the fluids also for this younger phase can be inferred by the palaeogeographic position of the Montalto Dora sector in the distal part of the Adria margin, where deep-marine conditions were already established at the time of this hydrothermal circulation (late Early Jurassic, see below). The interpretation of an interaction with the crystalline basement is also supported by the Sr isotope values (Figure 15): both a sample of a void-filling dolomite cement (MD1511) and a sample of a coarse-grained dolostone clast (MD1540) gave values much higher than any Mesozoic seawater, thus, pointing to a contribution by alteration processes of Rb-bearing minerals such as feldspars in metamorphic and volcanic/volcanosedimentary rocks.

In this sector, magmatic and metamorphic rocks of the basement have undergone Alpine metamorphic overprint with the formation of prehnite–pumpellyite–actinolite facies paragenesis (Biino & Compagnoni, 1989). Zingg et al. (1976) reported an anchizone/epizone metamorphism in Jurassic sediments from the Montalto Dora area, based on illite crystallinity data. However, the studied sedimentary rocks do not show evidence of recrystallization. The highest clumped isotope temperatures of up to 350°C recorded in two dolomite samples are higher than what would be expected from the above-cited. The cause of this discrepancy is not clear, it may lay in the temperature calibration, and requires further studies. However, the clumped isotope data show that different dolomites may have different behaviour upon reordering and that dolomite in certain instances can preserve temperatures close to peak metamorphic conditions, and thus, can be used as a valuable tool to reconstruct the tectonic history in low-temperature metamorphic terrains. The U/Pb ages, which preserved Triassic and Jurassic ages in spite of the Alpine metamorphism, show that these phases behaved as a closed system, even under relatively high temperatures, and did not recrystallize. As the U/Pb system is much more prone to alteration than the oxygen isotopes in the carbonates, we conclude that the oxygen isotope signature of the cements was not affected by exchange with metamorphic fluids, and thus, they preserved the original oxygen isotope signature. Finally, it is also noteworthy that the temperature of homogenization of the fluid inclusions is consistent with those measured in the other two sectors, indicating that they have preserved the original temperature in spite of the late Alpine overprint.

6.2.4 | Age of the hydrothermal events

In the Montalto Dora sector, two different hydrothermal circulation events, which pre- and post-dated the deposition of MUF-AM, have been documented. Although no chronostratigraphic data are available for the MUF, some biostratigraphic information is available on the infillings of the dykes that pre-date the deposition of the MUF sediments. Fossil-bearing carbonate sediments within these dykes allow dating of the first phase of fracturing to the earliest Sinemurian (Baggio, 1965; Elter et al., 1966; Sturani, 1964). This opening phase was followed by a second one during which the siliciclastic sediments of the MUF-AM filled the fissures. Within the Muriaglio Fm. sediments, the U/Pb dating of three coarsely crystalline dolostone clasts records the recrystallization (documented by the pervasive swarms of veinlets) of different portions of the original Middle Triassic finely crystalline dolostones, before their erosion and sedimentation as clasts within the Muriaglio Fm. sediments. One clast showed a Rhaetian–Sinemurian age (MD1513, 199.2 ± 7.4 Ma), whereas two indicated a late Pliensbachian–Toarcian age (MD1540, 182.1 ± 5.7 Ma; MD1663 179.6 ± 5.3 Ma; Figure 15). These data indicate that the hydrothermal fluid circulation must have started at the Triassic–Jurassic boundary and continued up to the latest Pliensbachian–Toarcian, causing the local recrystallization

of the SSD and the opening of the dolomite- and quartz-cemented Type 1 veins (Figure 18). The base of the Muriaglio Formation must be younger than the youngest clast age, and thus, considering the possible uncertainties, it has to be latest Pliensbachian–Toarcian. It is worth to stress that, despite the common stratigraphic position and closely similar lithological features, the Muriaglio Formation is possibly slightly younger than the San Quirico Sandstones of the Monte Fenera–Sostegno sector. Moreover, Type 2 veins, whose features document circulation within a semi-consolidated sediment, document that hydrothermal fluids kept on flowing through the stratigraphic succession shortly after the beginning of the sedimentation of the Muriaglio Formation, that is, likely in the Toarcian.

6.3 | Summary discussion

The data presented document the circulation of hot fluids interacting with sediments located at shallow burial depths in the westernmost part of the Adriatic margin from the latest Triassic to the Toarcian. Temperatures in excess of 100°C may be related to deep fluid circulation and anomalously high heat fluxes, or a combination of both. A regional heating event in the 215–200 Ma interval has indeed been previously documented in the middle and lower crust (Ivrea–Verbano Zone: Mazzucchelli et al., 2010; Schaltegger et al., 2015; Zanetti et al., 2013) and in the upper crust of the Western Southalpine Domain. Here, Beltrando et al. (2015) already postulated a regional fluid flow at shallow crustal levels as the possible mechanism accounting for the thermal anomaly. The onset of the thermal anomaly was coeval with a regional-scale diffuse rifting stage of the Adriatic margin, well recorded by the sedimentary evolution of the Lombardian basin and the whole eastern Southalpine margin (i.e. to the east of the study area; Berra et al., 2009; Bertotti et al., 1993). In the Sostegno area, the thermochronological data by Beltrando et al. (2015) on Permian volcanics samples imply an elevated geothermal gradient around 60°C/km at the Triassic–Jurassic boundary. However, no evidence of this event has been detected at Monte Fenera–Sostegno. There, only a second late Pliensbachian stage is documented by dolomite-filled veins and cavities. This could be explained by the fact that, even if the anomalously high geothermal gradient at the Triassic–Jurassic boundary could represent a favourable factor for hydrothermal activity in the upper crust, the absence of deep and active faults in this limited sector at that time impeded the activation of hydrothermal cells. The latter were effective along main rift master faults, so not affecting the study area and possibly located more to the East.

Conditions changed about 20 Myr later, in the late Pliensbachian. A thermal relaxation probably occurred, although it seems reasonable to infer a geothermal gradient still considerably higher than 30°C/km, but a new extensional tectonic cycle had started. At the scale of the entire Adriatic palaeomargin, in fact, a shift of the rifting tectonics from the Lombardian Basin to the westernmost sectors occurred in the late Pliensbachian–Toarcian (Beltrando et al., 2015; Berra et al., 2009). The Fenera–Sostegno area corresponded to the necking zone, where the crust of the proximal margin thinned through crustal-scale extensional faults towards the distal margin. Very rapid exhumation along these faults has been documented by (U-Th)/He thermochronology data on detrital zircons in the San Quirico Sandstones (Beltrando et al., 2015). Such deep and active faults, and the related fracture systems, indeed could represent a very effective plumbing system both for descending marine and meteoric waters that could reach a few kilometres of depth in the crust, and for the upflowing hydrothermal fluids, as reported in other comparable tectonic settings (Hirani et al., 2018; Hollis et al., 2017; Incerpi, Manatschal, et al., 2020; Incerpi, Martire, et al., 2020; Shelton et al., 2019) (Figure 20).

To the west, in the Montalto Dora sector, two rift-related fluid circulations are documented by recrystallized dolomite clasts (Figure 15) and by Type 2 veins cutting through the MUF-AM (Figures 12 and 18). The first circulation occurred at the Triassic–Jurassic boundary (U/Pb age on sample MD1513; in Figure 15), and the second one at the latest Pliensbachian–Toarcian (two U/Pb age data on samples MD1540 and MD1663; Figure 15). This sector corresponded to a more distal portion of the margin that marked the transition from the necking zone to the hyperextended termination of the continental margin facing the mantle exhumation zone (Ferrando et al., 2004). In comparable tectonic settings, different authors calculated high palaeogeothermal gradients in excess of 70°C/km (Pinto et al., 2015; Salardon et al., 2017). The very high geothermal gradient and active low- and high-angle faults provided the ideal conditions to activate an active hydrothermal system in the latest Pliensbachian–Toarcian (Figure 20).

Recently, fluids involved in the alteration/carbonatation of mafic and ultramafic rocks have been proposed as a possible source of Mg for dolomitization processes (e.g. Koeashidayatullah et al., 2020; Lavoie et al., 2014). In hyperextended continental distal margins, such Mg-enriched fluids are derived from seawater serpentinization of mantle peridotite (e.g. Debure et al., 2019; Lagabrielle et al., 2019). In these settings, the upflow of Mg-enriched fluids can occur from the first phases of crustal extension, that is, well in advance of the eventual hyperextension and mantle exhumation. They are related to serpentinization at depth of mantle peridotite by fluids infiltrating along crustal-scale fault zones (Pinto et al., 2015, 2017). As the Montalto Dora sector in the late Early Jurassic was located on a considerably thinned continental crust, a contribution

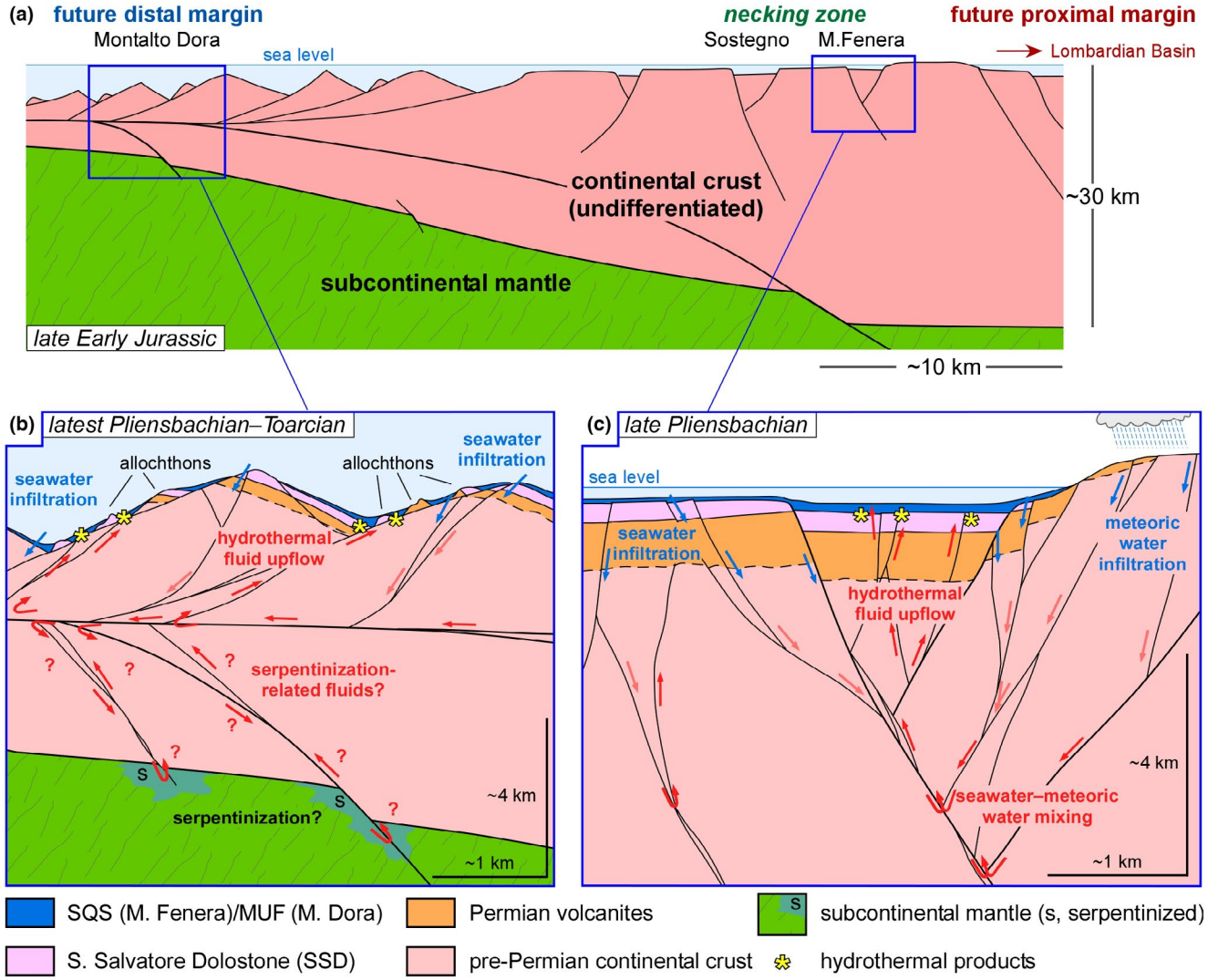

FIGURE 20 Conceptual model of hydrothermal circulation. (a) Ideal cross section across the future Adriatic palaeomargin in the late Early Jurassic (partly modified from Beltrando et al., 2015; Ferrando et al., 2004), showing the position of the zoomed areas in (b) and (c). (b and c) Schematic representation of the hypothetical origin and circulation pathways of hydrothermal fluids in the Montalto Dora (b) and Monte Fenera (c) areas; blue and red arrows represent cold descending and hot ascending fluids respectively

of Mg-enriched fluids, derived from deeply infiltrated seawater, which reacted with the top of the mantle, can be envisaged (Figure 20). However, the available geochemical dataset for Montalto Dora hydrothermal dolomites (Sr, C and O isotopes) bears a clear crustal signature, thus not providing any evidence for a contribution of mantle-reacted fluids. Testing this hypothesis would, thus, require additional data such as trace element or Mg isotope geochemistry (e.g. Lavoie et al., 2014).

The documented change in the paragenesis of hydrothermal veins from the necking zone (only dolomite at Monte Fenera–Sostegno) to the distal margin (dolomite + calcite + quartz at Montalto Dora) probably mirrors a difference in fluid flow pathways and fluid–rock interactions along the margin. In both settings, hydrothermal systems were fed by seawater, possibly partly mixed with meteoric waters at Monte Fenera–Sostegno. The seawater flowed downward along fault cores and associated damage zones, with resulting heating (Figure 20). Along detachment faults, flow paths through basement rocks are longer than in high-angle normal faults. Consequently, the interaction of fluids with silicate minerals is more prolonged, resulting in dissolved silica enrichment. A similar evolution has been recently documented in another part of the Adriatic palaeomargin, along the 'Grisons transect' in the Austroalpine units of southern Switzerland (Incerpi et al., 2017, 2018; Incerpi, Martire, et al., 2020).

The observed O and Sr isotope composition variability could be explained, in addition to the meteoric water contribution suggested for the Fenera–Sostegno area, also by complex patterns of fluid circulation in the crust in space and time. As suggested by Bons et al. (2014), surface fluids may

have a very long (tens of Myr) history of penetration into the crust, where the oldest fluids reach the greatest depths and younger fluids remain for shorter times at shallower depths. Temperatures and times of fluid–rock interactions/exchanges/equilibrations vary with depth and result in fluids with different temperatures, salinities, trace element and isotopic composition. These fluids are stored at different levels of the crustal column until conduits, such as faults and fractures, are generated in the crust, allowing overpressured fluids with different physic-chemical properties to flow upward and mix to variable degrees. In the study area, several stages of fluid infiltration from the surface, also aided by faulting, can be envisaged from the Permian to the earliest Jurassic first stage of rifting. However, it was probably only during the Pliensbachian stage of focussing of fault activity and crustal thinning that suitable pathways were generated for the release of fluids stored at variable levels of the crust.

7 | CONCLUDING STATEMENTS

This study investigates hydrothermal fluid circulation within the upper crust of the Adriatic continental margin of the Alpine Tethys during Jurassic extensional rifting. The products of this circulation in the Middle Triassic–Lower Jurassic pre- and syn-rift successions of the Western Southalpine Domain are mainly represented by vein and breccia cements, as well as a local dolomitization and silicification of the host rocks. Multidisciplinary investigation in the Monte Fenera–Sostegno and in the Montalto Dora areas, respectively, corresponding to the necking and hyperextended distal zone of the palaeomargin, allowed us to constrain the character, timing and evolution of the hydrothermal circulation:

- Hydrothermal fluids were relatively hot, 80–130°C, overpressured and circulated in a plumbing system developed along rift-related fault and fracture zones penetrating for some kilometres into basement rocks. The products of this circulation formed in pre- and syn-rift sediments in a very shallow burial setting, possibly up to the sediments–seawater interface.
- The hydrothermal systems were fed by seawater, with a possible local contribution of meteoric waters. Fluid composition was modified through interaction with the crystalline basement rocks during deep circulation.
- Stratigraphic and petrographic constraints and U–Pb radiometric dating point to at least two events of hydrothermal fluid circulation, which started with the first rifting stage in the latest Triassic, possibly related to anomalous heat fluxes linked to regional-scale thermal events already documented at deeper crustal levels. Hydrothermal activity lasted at least until the late Pliensbachian–Toarcian, when rifting tectonics were focused on the westernmost sector of the Adriatic palaeomargin (Montalto Dora sector) and led to crustal hyperextension.
- The different paragenesis of hydrothermal veins documents a compositional evolution from carbonate-dominated fluids in the necking zone (Monte Fenera–Sostegno) to carbonate- and silica-bearing fluids in the distal margin (Montalto Dora). This could reflect longer flow paths of the hydrothermal fluids along detachment faults, resulting in stronger interaction with crystalline silicate-rich rocks. This model of time and space variations in tectonically controlled fluid circulation in rift continental settings seems to confirm what has been recently proposed in another portion of the same margin (i.e. the Austroalpine Domain) and this process could be more frequent in hyperextended margins than reported to date.

ACKNOWLEDGEMENTS

We thank Cathy Hollis, Nicolas Beaudoin, Philippe Boulvais and an anonymous reviewer, whose comments and suggestions greatly improved an earlier version of the manuscript. This research was developed in the frame of the project ‘Probing the depth: termo-tectonic evolution of hyperextended rifted margins' (financed by Compagnia di San Paolo and University of Torino, P.I.: Simona Ferrando, formerly Marco Beltrando). The research was also supported by the University of Torino (ex 60% funds) and by the CNR-IGG (National Research Council of Italy, Institute of Geosciences and Earth Resources, Torino unit). We dedicate this article to the memory of our friend and colleague Marco Beltrando, who inspired this research and introduced some of us to the geology of the westernmost part of the Adriatic palaeomargin.

PEER REVIEW

The peer review history for this article is available at https://publons.com/publon/10.1111/bre.12594.

DATA AVAILABILITY STATEMENT

The data that support the findings of this study are available from the corresponding author upon reasonable request.

ORCID

C. Bertok https://orcid.org/0000-0001-9793-8078
S. Agostini https://orcid.org/0000-0002-2060-0359
S. M. Bernasconi https://orcid.org/0000-0001-7672-8856

REFERENCES

Ahrendt, H. (1972). Zur Stratigraphie, Petrographie und zum tektonischen Aufbau der Canavese-Zone und ihrer Lage zum Insubrischen Linie zwischen Biella und Cuorgné (Norditalien). *Göttinger Arbeiten Zur Geologie Und Paläontologie*, *11*, 1–89.

Baggio, P. (1965). Caratteri stratigrafici e strutturali del Canavese s.s. nella zona di Montalto Dora. Mem. Ist. Geol. Mineral. Univ. Padova, *25*, 1–25.

Barale, L., Bertok, C., d'Atri, A., Piana, F., Bernasconi, S., Czuppon, G., Palcsu, L., Gerdes, A., Birgel, D., & Martire, L. (2021). U-Pb dating and geochemical constraints to Early Cretaceous hydrothermal dolomitization in the Provençal Domain (Maritime Alps, NW Italy–SE France). *Ofioliti*, *46*(2), 131–149.

Barale, L., Bertok, C., Salih, T. N., d'Atri, A., Martire, L., Piana, F., & Préat, A. (2016). Very hot, very shallow hydrothermal dolomitization: An example from the Maritime Alps (NW Italy-SE France). *Sedimentology*, *63*, 2037–2065.

Beltrando, M., Stockli, D. F., Decarlis, A., & Manatschal, G. (2015). A crustal-scale view at rift localization along the fossil Adriatic margin of the Alpine Tethys preserved in NW Italy. *Tectonics*, *34*(9), 1927–1951. https://doi.org/10.1002/2015TC003973

Bernasconi, S. M., Müller, I. A., Bergmann, K. D., Breitenbach, S. F., Fernandez, A., Hodell, D. A., Jaggi, M., Meckler, A. N., Millan, I., & Ziegler, M. (2018). Reducing uncertainties in carbonate clumped isotope analysis through consistent carbonate-based standardization. *Geochemistry, Geophysics, Geosystems*, *19*(9), 2895–2914. https://doi.org/10.1029/2017GC007385

Bernoulli, D. (1964). Zur Geologie des Monte Generoso. Ein Beitrag zur Kenntnis der sudalpinen Sedimente. Beitr. Geol. Karte Schweiz., N.F., *118*, 134.

Berra, F., Galli, M. T., Reghellin, F., Torricelli, S., & Fantoni, R. (2009). Stratigraphic evolution of the Triassic-Jurassic succession in the Western Southern Alps (Italy): The record of the two-stage rifting on the distal passive margin of Adria. *Basin Research*, *21*, 335–353. https://doi.org/10.1111/j.1365-2117.2008.00384.x

Bertotti, G., Picotti, V., Bernoulli, D., & Castellarin, A. (1993). From rifting to drifting: Tectonic evolution of the South-Alpine upper crust from the Triassic to the Early Cretaceous. *Sedimentary Geology*, *86*(1–2), 53–76. https://doi.org/10.1016/0037-0738(93)90133-P

Biino, G., & Compagnoni, R. (1989). The Canavese Zone between the Serra d'Ivrea and the Dora Baltea River (Western Alps). *Eclogae Geologicae Helvetiae*, *82*(2), 413–427.

Bjørlykke, K. (1993). Fluid flow in sedimentary basins. *Sedimentary Geology*, *86*(1–2), 137–158. https://doi.org/10.1016/0037-0738(93)90137-T

Bjørlykke, K. (2010). *Petroleum geoscience* (p. 508). Springer-Verlag.

Bons, P. D., Fusswinkel, T., Gomez-Rivas, E., Markl, G., Wagner, T., & Walter, B. (2014). Fluid mixing from below in unconformity-related hydrothermal ore deposits. *Geology*, *42*(12), 1035–1038. https://doi.org/10.1130/G35708.1

Breitenbach, S. F. M., & Bernasconi, S. M. (2011). Carbon and oxygen isotope analysis of small carbonate samples (20 to 100 µg) with a GasBench II preparation device. *Rapid Communications in Mass Spectrometry*, *25*, 1910–1914.

Brigaud, B., Bonifacie, M., Pagel, M., Blaise, T., Calmels, D., Haurine, F., & Landrein, P. (2020). Past hot fluid flows in limestones detected by Δ47–(U-Pb) and not recorded by other geothermometers. *Geology*, *48*, 851–856. https://doi.org/10.1130/G47358.1

Clayton, R. N., Friedman, I., Graf, D. L., Mayeda, T. K., Meents, W. F., & Shimp, N. F. (1966). The origin of saline formation waters: I. Isotopic composition. *Journal of Geophysical Research*, *71*, 3869–3882.

Cohen, K. M., Finney, S. C., Gibbard, P. L., & Fan, J.-X. (2013). The ICS international chronostratigraphic chart. *Episodes*, *36*, 199–204. https://doi.org/10.18814/epiiugs/2013/v36i3/002

Davies, G. R., & Smith, L. B. Jr (2006). Structurally controlled hydrothermal dolomite reservoir facies: An overview. *AAPG Bulletin*, *90*, 1641–1690. https://doi.org/10.1306/05220605164

Debure, M., Lassin, A., Marty, N. C., Claret, F., Virgone, A., Calassou, S., & Gaucher, E. C. (2019). Thermodynamic evidence of giant salt deposit formation by serpentinization: An alternative mechanism to solar evaporation. *Scientific Reports*, *9*, 11720. https://doi.org/10.1038/s41598-019-48138-9

Decarlis, A., Beltrando, M., Manatschal, G., Ferrando, S., & Carosi, R. (2017). Architecture of the distal Piedmont-Ligurian rifted margin in NW Italy: Hints for a flip of the rift system polarity. *Tectonics*, *36*, 2388–2406. https://doi.org/10.1002/2017TC004561

Diamond, L. W., Wanner, C., & Waber, H. N. (2018). Penetration depth of meteoric water in orogenic geothermal systems. *Geology*, *46*(12), 1063–1066. https://doi.org/10.1130/G45394.1

Elisha, B., Nuriel, P., Kylander-Clark, A., & Weinberger, R. (2020). Towards in-situ U–Pb dating of dolomites. *Geochronology Discuss*. [preprint], https://doi.org/10.5194/gchron-2020-19, in review, 2020.

Elter, G., Elter, P., Sturani, C., & Weidmann, M. (1966). Sur la prolongation du Domaine Ligure de l'Apennin dans le Monferrat et les Alpes et sur l'origine de la nappe de la Simme s.l. des Préalpes Romandes et Chablaisiennes. *Archives Des Sciences*, *19*(3), 279–377.

Fantoni, R., Decarlis, A., & Fantoni, E. (2003). Mesozoic extension at the western margin of the Southern Alps (northern Piedmont, Italy). *Atti Tic. Sci. Terra*, *44*, 97–110.

Fantoni, R., & Scotti, P. (2003). Thermal record of the Mesozoic extensional tectonics in the Southern Alps. *Atti Tic. Sci. Terra* (serie speciale), *9*, 96–101.

Fernandez, A., Müller, I. A., Rodriguez-Sanz, L., van Dijk, I., Looser, N., & Bernasconi, S. M. (2017). Reassessment of the precision of carbonate clumped isotope measurements: Implications for calibrations and paleoclimate reconstructions. *Geochemistry, Geophysics, Geosystems*, *18*. 4375–4386. https://doi.org/10.1002/2017GC007106

Ferrando, S., Bernoulli, D., & Compagnoni, R. (2004). The Canavese zone (internal Western Alps): A distal margin of Adria. *Schweizerische Mineralogische Und Petrographische Mitteilungen*, *84*, 237–256.

Festa, A., Balestro, G., Borghi, A., De Caroli, S., & Succo, A. (2020). The role of structural inheritance in continental break-up and exhumation of Alpine Tethyan mantle (Canavese Zone, Western Alps). *Geoscience Frontiers*, *11*(1), 167–188. https://doi.org/10.1016/j.gsf.2018.11.007

Folk, R. L. (1962). Spectral subdivision of limestone types. In W. E. Ham (Ed.), *Classification of carbonate rocks* (pp. 62–84). AAPG.

Gerdes, A., & Zeh, A. (2006). Combined U-Pb and Hf isotope LA-(MC-)ICP-MS analyses of detrital zircons: Comparison with SHRIMP and new constraints for the provenance and age of an Armorican metasediment in Central Germany. *Earth and Planetary Science Letters*, *249*, 47–62. https://doi.org/10.1016/j.epsl.2006.06.039

Gerdes, A., & Zeh, A. (2009). Zircon formation versus zircon alteration – New insights from combined U-Pb and Lu-Hf in-situ La-ICP-MS analyses of Archean zircons from the Limpopo Belt. *Chemical Geology*, *261*(3–4), 230–243.

Goldstein, R. H., & Reynolds, T. J. (1994) Systematics of fluid inclusions in diagenetic minerals. SEPM Short Course 31, Tulsa, 199 p.

Govi, M. (1975). *Carta geologica del distretto vulcanico ad Oriente della bassa Val Sesia, Scala 1:25000*. CNR - Centro di studi sui problemi dell'Orogeno delle Alpi Occidentali.

Haeri-Ardakani, O., Al-Aasm, I., & Coniglio, M. (2013). Fracture mineralization and fluid flow evolution: An example from Ordovician-Devonian carbonates, southwestern Ontario, Canada. *Geofluids*, *13*, 1–20. https://doi.org/10.1111/gfl.12003

Handy, M. R. (1987). The structure, age and kinematics of the Pogallo fault zone - Southern Alps, Northwestern Italy. *Eclogae Geologicae Helvetiae*, *80*(3), 593–632.

Hirani, J., Bastesen, E., Boyce, A., Corlett, H., Eker, A., Gawthorpe, R., Hollis, C., Korneva, I., & Rotevatn, A. (2018). Structural controls on non fabric-selective dolomitization within rift-related basin-bounding normal fault systems: Insights from the Hammam Faraun Fault, Gulf of Suez, Egypt. *Basin Research*, *30*, 990–1014. https://doi.org/10.1111/bre.12290

Hitchon, B., & Friedman, L. (1969). Geochemistry and origin of formation waters in the western Canadian sedimentary basin. I. Stable isotopes of hydrogen and oxygen. *Geochimica Et Cosmochimica Acta*, *33*, 1321–1349.

Hoefs, J. (2018). *Stable isotope geochemistry* (8th ed., p. 437). Springer-Verlag.

Hollis, C., Bastesen, E., Boyce, A., Corlett, H., Gawthorpe, R., Hirani, J., Rotevatn, A., & Whitaker, F. (2017). Fault-controlled dolomitization in a rift basin. *Geology*, *45*, 219–222. https://doi.org/10.1130/G38s394.1

Incerpi, N., Manatschal, G., Martire, L., Bernasconi, S. M., Gerdes, A., & Bertok, C. (2020). Characteristics and timing of hydrothermal fluid circulation in the fossil Pyrenean hyperextended rift system: New constraints from the Chaînons Béarnais (W Pyrenees). *International Journal of Earth Sciences*, *109*, 1071–1093. https://doi.org/10.1007/s00531-020-01852-6

Incerpi, N., Martire, L., Bernasconi, S. M., Manatschal, G., & Gerdes, A. (2018). Silica-rich septarian concretions in biogenic silica-poor sediments: A marker of hydrothermal activity at fossil hyperextended rifted margins (Err nappe, Switzerland). *Sedimentary Geology*, *378*, 19–33. https://doi.org/10.1016/j.sedgeo.2018.10.005

Incerpi, N., Martire, L., Manatschal, G., & Bernasconi, S. M. (2017). Evidence of hydrothermal fluid flow in a hyperextended rifted margin: The case study of the Err nappe (SE Switzerland). *Swiss Journal of Geosciences*, *110*(2), 439–456. https://doi.org/10.1007/s00015-016-0235-2

Incerpi, N., Martire, L., Manatschal, G., Bernasconi, S. M., Gerdes, A., Czuppon, G., Palcsu, L., Karner, G. D., Johnson, C. A., & Figueredo, P. H. (2020). Hydrothermal fluid flow associated to the extensional evolution of the Adriatic rifted margin: Insights from the pre- to post-rift sedimentary sequence (SE Switzerland, N ITALY). *Basin Research*, *32*, 91–115. https://doi.org/10.1111/bre.12370

John, C. M., & Bowen, D. (2016). Community software for challenging isotope analysis: First applications of "Easotope" to clumped isotopes. *Rapid Communications in Mass Spectrometry*, *30*, 2285–2300.

Koeashidayatullah, A., Corlett, H., Stacey, J., Swart, P. K., Boyce, A., Robertson, H., Whitaker, F., & Hollis, C. (2020). Evaluating new fault-controlled hydrothermal dolomitization models: Insights from the Cambrian Dolomite, Western Canadian Sedimentary Basin. *Sedimentology*, *67*, 2945–2973. https://doi.org/10.1111/sed.12729

Lagabrielle, Y., Asti, R., Fourcade, S., Corre, B., Poujol, M., Uzel, J., Labaume, P., Clerc, C., Lafay, R., Picazo, S., & Maury, R. (2019). Mantle exhumation at magma-poor passive continental margins. Part I. 3D architecture and metasomatic evolution of a fossil exhumed mantle domain (Urdach lherzolite, north-western Pyrenees, France). *Bulletin De La Société Géologique De France*, *190*, 8.

Land, L. S., & Prezbindowski, D. R. (1981). The origin and evolution of saline formation waters, Lower Cretaceous carbonates, south–central Texas and southern New Mexico. *Journal of Hydrogeology*, *54*, 51–74.

Lapponi, F., Bechstädt, T., Boni, M., Banks, D. A., & Schneider, J. (2014). Hydrothermal dolomitization in a complex geodynamic setting (Lower Palaeozoic, northern Spain). *Sedimentology*, *61*, 411–443. https://doi.org/10.1111/sed.12060

Lavoie, D., Jackson, S., & Girard, I. (2014). Magnesium isotopes in high-temperature saddle dolomite cements in the lower Paleozoic of Canada. *Sedimentary geology*, *305*, 58–68. https://doi.org/10.1016/j.sedgeo.2014.03.002

Leach, D. L., Bradley, D. C., Huston, D., Pisarevsky, S. A., Taylor, R. D., & Gardoll, S. J. (2010). Sediment-hosted lead-zinc deposits in earth history. *Economic Geology*, *105*(3), 593–625. https://doi.org/10.2113/gsecongeo.105.3.593

López-Horgue, M. A., Iriarte, E., Schröeder, S., Fernández-Mendiola, P. A., Caline, B., Corneyllie, H., Frémont, J., Sudrie, M., & Zerti, S. (2010). Structurally controlled hydrothermal dolomites in Albian carbonates of the Asón valley, Basque Cantabrian Basin, Northern Spain. *Marine and Petroleum Geology*, *27*, 1069–1092.

Ludwig, K. R. (2009) *Isoplot/Ex Ver 3.71: A geochronological toolkit for Microsoft Excel*. Berkeley Geochronology Center Special Publication.

Machel, H. G. (2004) Concepts and models of dolomitization: A critical reappraisal. In C. J. R. Braithwaite, G. Rizzi, & G. Darke (Eds.), *The geometry and petrogenesis of dolomite hydrocarbon reservoirs* (Vol. *235*, pp. 7–63). Geol. Soc. London, Sp. Pub.

Machel, H. G., & Lonnee, J. (2002). Hydrothermal dolomite – A product of poor definition and imagination. *Sedimentary Geology*, *152*, 163–171. https://doi.org/10.1016/S0037-0738(02)00259-2

Mangenot, X., Gasparrini, M., Gerdes, A., Bonifacie, M., & Rouchon, V. (2018). An emerging thermochronometer for carbonate-bearing rocks: Δ47 /(U-Pb). *Geology*, *46*(12), 1067–1070. https://doi.org/10.1130/G45196.1

Martín-Martín, J. D., Travé, A., Gomez-Rivas, E., Salas, R., Sizun, J.-P., Vergés, J., Corbella, M., Stafford, S. L., & Alfonso, P. (2015). Fault-controlled and stratabound dolostones in the Late Aptian–earliest Albian Benassal Formation (Maestrat Basin, E Spain): Petrology and geochemistry constrains. *Marine and Petroleum Geology*, *65*, 83–102. https://doi.org/10.1016/j.marpetgeo.2015.03.019

Martire, L., Bertok, C., d'Atri, A., Perotti, E., & Piana, F. (2014). Selective dolomitization by syntaxial overgrowth around detrital dolomite nuclei: A case from the Jurassic of the Ligurian Briançonnais (Ligurian Alps). *Journal of Sedimentary Research*, *84*, 40–50.

Masini, E., Manatschal, G., & Mohn, G. (2013). The Alpine Tethys rifted margin: Reconciling old and new ideas to understand the stratigraphic architecture of magma-poor rifted margins. *Sedimentology*, *60*, 174–196.

Mazzucchelli, M., Zanetti, A., Rivalenti, G., Vannucci, R., Correia, C. T., & Tassinari, C. C. G. (2010). Age and geochemistry of mantle peridotites and diorite dykes from the Baldissero body: Insights into the Paleozoic-Mesozoic evolution of the Southern Alps. *Lithos*, *119*, 485–500. https://doi.org/10.1016/j.lithos.2010.08.002

McArthur, J. M., Howarth, R. J., & Shields, G. A. (2012). Strontium isotope stratigraphy. In F. M. Gradstein, J. G. Ogg, M. Schmitz, & G. Ogg (Eds.), *The geologic time scale 2012* (pp. 127–144). Elsevier.

Meckler, A. N., Ziegler, M., Millán, M. I., Breitenbach, S. F. M., & Bernasconi, S. M. (2014). Long-term performance of the Kiel carbonate device with a new correction scheme for clumped isotope measurements. *Rapid Communications in Mass Spectrometry*, *28*, 1705–1715. https://doi.org/10.1002/rcm.6949

Mohn, G., Manatschal, G., Müntener, O., Beltrando, M., & Masini, E. (2010). Unravelling the interaction between tectonic and sedimentary processes during lithosphere thinning in the Alpine Tethys margins. *International Journal of Earth Sciences*, *99*, 75–101.

Motte, G., Hoareau, G., Callot, J. P., Révillon, S., Piccoli, F., Calassou, S., & Gaucher, E. C. (2021). Rift and salt-related multi-phase dolomitization: Example from the northwestern Pyrenees. *Marine and Petroleum Geology*, *126*, 104932. https://doi.org/10.1016/j.marpetgeo.2021.104932

Müller, I. A., Fernandez, A., Radke, J., Dijk, J. V., Bowen, D., Schwieters, J., & Bernasconi, S. M. (2017). Carbonate clumped isotope analyses with the long-integration dual-inlet (LIDI) workflow: Scratching at the lower sample weight boundaries. *Rapid Communications in Mass Spectrometry*, *2*, 1057–1066. https://doi.org/10.1002/rcm.7878

Müller, I. A., Rodriguez-Blanco, J. D., Storck, J.-C., do Nascimento, G. S., Bontognali, T. R. R., Vasconcelos, C., Benning, L. G., & Bernasconi, S. M. (2019). Calibration of the oxygen and clumped isotope thermometers for (proto-)dolomite based on synthetic and natural carbonates. *Chemical Geology*, *525*, 1–17. https://doi.org/10.1016/j.chemgeo.2019.07.014

Nunn, E. V., & Price, G. D. (2010). Late Jurassic (Kimmeridgian–Tithonian) stable isotopes ($\delta^{18}O$, $\delta^{13}C$) and Mg/Ca ratios: New palaeoclimate data from Helmsdale, northeast Scotland. *Palaeogeography, Palaeoclimatology, Palaeoecology*, *292*, 325–335.

O'Neil, J. R., Clayton, R. N., & Mayeda, T. K. (1969). Oxygen isotope fractionation in divalent metal carbonates. *Journal of Chemistry and Physics*, *51*, 5547–5558. https://doi.org/10.1063/1.1671982

Paradis, S., Hannigan, P., & Dewing, K. (2007) Mississippi Valley-type lead-zinc deposits. In W. D. Goodfellow (Ed.), *Mineral deposits of Canada: A synthesis of major deposit-types, district metallogeny, the evolution of geological provinces, and exploration methods* (Vol. *5*, pp. 185–203). Geological Association of Canada, Mineral Deposits Division, Special Publication.

Piana, F., Barale, L., Compagnoni, R., d'Atri, A., Fioraso, G., Irace, A., Mosca, P., Tallone, S., Monegato, G., & Morelli, M. (2017). Geological Map of Piemonte Region at 1:250,000 scale. Explanatory Notes. Acc. *Sc. Torino. Memorie Sc. Fis.*, *41*, 3–143.

Piana, F., Fioraso, G., Irace, A., Mosca, P., d'Atri, A., Barale, L., Falletti, P., Monegato, G., Morelli, M., Tallone, S., & Vigna, G. B. (2017). Geology of Piemonte region (NW Italy, Alps-Apennines interference zone). *Journal of Maps*, *13*(2), 395–405. https://doi.org/10.1080/17445647.2017.1316218

Pinto, V. H. G., Manatschal, G., Karpoff, A. M., Ulrich, M., & Viana, A. R. (2017). Seawater storage and element transfer associated with mantle serpentinization in magma-poor rifted margins: A quantitative approach. *Earth and Planetary Science Letters*, *459*, 227–237. https://doi.org/10.1016/j.epsl.2016.11.023

Pinto, V. H. G., Manatschal, G., Karpoff, A. M., & Viana, A. R. (2015). Tracing mantle-reacted fluids in magma-poor rifted margins: The example of Alpine Tethyan rifted margins. *Geochemistry, Geophysics, Geosystems*, *16*, 3271–3308.

Pirajno, F. (2009). *Hydrothermal processes and mineral systems* (p. 1250). Springer-Verlag.

Podlaha, O. G., Mutterlose, J., & Veizer, J. (1998). Preservation of $\delta^{18}O$ and $\delta^{13}C$ in belemnite rostra from the Jurassic/Early Cretaceous successions. *American Journal of Science*, *298*, 324–347.

Roberts, N. M. W., Rasbury, E., Troy, P., Randall, R., Smith, C. J., Horstwood, M. S. A., & Condon, D. J. (2017). A calcite reference material for LA-ICP-MS U-Pb geochronology. *Geochemistry Geophysics Geosystems*, *18*(7), 2807–2814. https://doi.org/10.1002/2016GC006784

Rosenbaum, J., & Sheppard, S. M. (1986). An isotopic study of siderites, dolomites and ankerites at high temperatures. *Geochimica Et Cosmochimica Acta*, *50*, 1147–1150.

Salardon, R., Carpentier, C., Bellahsen, N., Pironon, J., & France-Lanord, C. (2017). Interactions between tectonics and fluid circulations in an inverted hyper-extended basin: Example of Mesozoic carbonate rocks of the western North Pyrenean Zone (Chainons Béarnais, France). *Marine and Petroleum Geology*, *80*, 563–586.

Salih, N., Mansurbeg, H., Kolo, K., Gerdes, A., & Préat, A. (2019). In situ U-Pb dating of hydrothermal diagenesis in tectonically controlled fracturing in the Upper Cretaceous Bekhme Formation, Kurdistan Region-Iraq. *International Geologiy Review*, *62*, 2261–2279. https://doi.org/10.1080/00206814.2019.1695151

Salomon, E., Rotevatn, A., Kristensen, T. B., Grundvåg, S.-A., Henstra, G. A., Meckler, A. N., Albert, R., & Gerdes, A. (2020). Fault-controlled fluid circulation and diagenesis along basin-bounding fault systems in rifts – Insights from the East Greenland rift system. *Solid Earth*, *11*, 1987–2013. https://doi.org/10.5194/se-11-1987-2020

Schaltegger, U., Ulianov, A., Muntener, O., Ovtcharova, M., Peytcheva, I., Vonlanthen, P., Vennemann, T., Antognini, M., & Girlanda, F. (2015). Megacrystic zircon with planar fractures in miaskite-type nepheline pegmatites formed at high pressures in the lower crust (Ivrea Zone, Southern Alps, Switzerland). *American Mineralogist*, *100*, 83–94. https://doi.org/10.2138/am-2015-4773

Shah, M. M., Nader, F. H., Garcia, D., Swennen, R., & Ellam, R. (2012). Hydrothermal dolomites in the early Albian (Cretaceous) platform carbonates (NW Spain): Nature and origin of dolomites and dolomitising fluids. *Oil & Gas Science and Technology*, *67*(1), 97–122. https://doi.org/10.2516/ogst/2011174

Shelton, K. I., Hendry, J. P., Gregg, J. M., Truesdale, J. P., & Somerville, I. D. (2019). Fluid circulation and fault- and fracture-related diagenesis in Mississippian synrift carbonate rocks on the northeast margin of the metalliferous Dublin Basin, Ireland. *Journal of Sedimentary Research*, *89*, 508–536.

Sinigoi, S., Quick, J. E., Demarchi, G., & Klötzli, U. S. (2016). Production of hybrid granitic magma at the advancing front of basaltic underplating: Inferences from the Sesia Magmatic System (south-western Alps, Italy). *Lithos*, *252–253*, 109–122. https://doi.org/10.1016/j.lithos.2016.02.018

Stolper, D. A., & Eiler, J. M. (2015). The kinetics of solid-state isotope-exchange reactions for clumped isotopes. A study of inorganic calcites and apatites from natural and experimental samples. *American Journal of Science*, *315*, 363–411. https://doi.org/10.2475/05.2015.01

Sturani, C. (1964). Prima segnalazione di Ammoniti nel Lias del Canavese. *Rend. Accad. Lincei*, *37*, 482–483.

Swennen, R., Dewit, J., Fierens, E., Muchez, P., Shah, M., Nader, F., & Hunt, D. (2012). Multiple dolomitization events along the Pozalagua Fault (Pozalagua Quarry, Basque-Cantabrian Basin, Northern Spain). *Sedimentology*, *59*, 1345–1374. https://doi.org/10.1111/j.1365-3091.2011.01309.x

Warren, J. (2000). Dolomite: Occurrence, evolution and economically important associations. *Earth Science Reviews*, *52*, 1–81.

Wozniak, J. (1977). *Contribution à l'étude géologique des Alpes Occidentales internes: La région du Canavese* (p. 146, PhD thesis). Pierre et Marie Curie University.

Yardley, B. W. D. (2005). Metal concentrations in crustal fluids and their relationship to ore formation. *Economic Geology*, *100*, 613–632.

Yardley, B. W. D., & Bodnar, R. J. (2014). Fluids in the continental crust. *Geochemical Perspectives*, *3*(1), 1–127. https://doi.org/10.7185/geochempersp.3.1

Zanetti, A., Mazzucchelli, M., Sinigoi, S., Giovanardi, T., Peressini, G., & Fanning, M. (2013). SHRIMP U-Pb zircon Triassic intrusion age of the Finero mafic complex (Ivrea–Verbano Zone, Western Alps) and its geodynamic implications. *Journal of Petrology*, *54*, 2235–2265. https://doi.org/10.1093/petrology/egt046

Zingg, A., Hunziker, J. C., Frey, M., & Ahrendt, H. (1976). Age and degree of metamorphism of the Canavese Zone and of the sedimentary cover of the Sesia Zone. *Schweizerische Mineralogische Und Petrographische Mitteilungen*, *56*, 361–375.

SUPPORTING INFORMATION

Additional supporting information may be found online in the Supporting Information section.

How to cite this article: Barale, L., Bertok, C., d'Atri, A., Mantovani, A., Martire, L., Agostini, S., Bernasconi, S. M., Gerdes, A., & Ferrando, S. (2021). Syn-rift hydrothermal circulation in the Mesozoic carbonates of the western Adriatic continental palaeomargin (Western Southalpine Domain, NW Italy). *Basin Research*, 00, 1–32. https://doi.org/10.1111/bre.12594